DISSERTATIONS IN
FORESTRY AND
NATURAL SCIENCES

**Tero Vatanen**

# *Multi-leaf Collimation of Electron Beams with Monte Carlo Modelling and Dose Calculation*

## *Special Reference to Dosimetry and Build-up Dose*

Publications of the University of Eastern Finland
*Dissertations in Forestry and Natural Sciences*

UNIVERSITY OF
EASTERN FINLAND

**TERO VATANEN**

# *Multi-leaf Collimation of Electron Beams with Monte Carlo Modelling and Dose Calculation*

## *–Special Reference to Dosimetry and Build-up Dose*

Publications of the University of Eastern Finland
Dissertations in Forestry and Natural Sciences
No 33

Academic Dissertation
To be presented by permission of the Faculty of Science and Forestry for public examination in the Auditorium MET in Mediteknia Building at the University of Eastern Finland, Kuopio, on June, 3, 2011,
at 12 o'clock noon.

Cancer Center, Kuopio University Hospital
Department of Applied Physics, University of Eastern Finland

Kopijyvä Oy
Kuopio, 2011
Editor: Prof. Pertti Pasanen

Distribution:
University of Eastern Finland Library / Sales of publications
P.O. Box 107, FI-80101 Joensuu, Finland
tel. +358-50-3058396
http://www.uef.fi/kirjasto

ISBN: 978-952-61-0433-1 (printed)
ISSN: 1798-5668
ISSNL: 1798-5668
ISBN: 978-952-61-0434-8 (pdf)
ISSN: 1798-5676

Author's address:
Kuopio University Hospital
Cancer Center
P.O.Box 1777
70211 KUOPIO
FINLAND
email: terov@student.uef.fi

Supervisors:
Docent Tapani Lahtinen, Ph.D.
Kuopio University Hospital
Cancer Center
P.O.Box 1777
70211 KUOPIO
FINLAND
email: tapani.lahtinen@kuh.fi

Erik Traneus, Ph.D.
RaySearch Laboratories AB
Sveavägen 25
111 34 STOCKHOLM
SWEDEN
email: erik.traneus@raysearchlabs.com

Reviewers:
Adjunct Professor Anders Ahnesjö, Ph.D.
Uppsala University
Department of Radiology, Oncology and
Radiation Sciences
Akademiska sjukhuset
751 85 UPPSALA
SWEDEN
email: anders.ahnesjo@onkologi.uu.se

Docent Simo Hyödynmaa, Ph.D.
Tampere University Hospital
Department of Oncology
P.O.Box 2000
33521 TAMPERE
FINLAND
email: simo.hyodynmaa@pshp.fi

Opponent:
Docent Mikko Tenhunen, Ph.D.
Helsinki University Central Hospital
Department of Oncology
P.O.Box 180
00029 HUS
FINLAND
email: mikko.tenhunen@hus.fi

## ABSTRACT

Tumours and other superficial targets are often treated with electron beams in radiotherapy. The build-up dose and the therapeutic range of electrons are controlled by selecting the electron energy and by using a water-equivalent bolus placed on the skin. Currently, the shaping of clinical electron beams is often done via low melting point alloy block inserts individually made for each patient. However, leaf based collimation with an electron multi-leaf collimator (eMLC) might represent a more practical option. In the present study, the possibility of using a new eMLC as an add-on device to an existing linear accelerator was investigated. The main focus was on the dosimetric properties and feasibility of modelling the eMLC beam with a parametrized Monte Carlo (MC) beam model. Secondly, the effect of eMLC leaf geometry on build-up dose of narrow beams was studied with the aim of replacing a conventional bolus with eMLC. In this work, the Voxel Monte Carlo++ (VMC++) algorithm was demonstrated to be very accurate in the dose calculation of the eMLC beam. Compared against measurements in water, the agreement was within 2% or 2 mm in 88% of the calculated voxels. The maximum dose from eMLC beams was only slightly higher in the target volume when compared with the current insert-based collimation in the chest wall irradiation of breast cancer. Narrow eMLC beams with a field size 1×10 cm$^2$ have a markedly higher build-up dose compared to a large field meaning that it was possible to replace a bolus by the combination of several narrow eMLC fields. Depending on the eMLC leaf end shape, the surface dose at 0.5 mm depth can be up to 90% of the dose maximum with abutting narrow beams which is approximately 25% higher than the surface dose with an open field and is comparable to electron beams used with a with bolus material. The add-on type eMLC results in only marginal differences compared with the present technique for electron beam collimation with block inserts. The novel beam model together with VMC++ enables patient dose calculations and may be developed for clinical use.

*National Library of Medicine Classification: QT 36, WN 105, WN 250, WN 250.5.R2, WN 665*
*INSPEC Thesaurus: radiation therapy; electron beams; beam handling equipment; collimators; linear accelerators; dosimetry; modelling; Monte Carlo methods*
*Yleinen suomalainen asiasanasto: sädehoito; ionisoiva säteily; säteilyannokset; hiukkaskiihdyttimet; mallintaminen; Monte Carlo -menetelmät*

*To Vilma, Miina and Minna*

# Acknowledgements

The work in this thesis was conducted during 2005–11 in Kuopio University Hospital, Cancer Center and finalized in 2008–11 in North Karelia Central Hospital, Oncology Clinic. I want to thank my supervisors, Docent Tapani Lahtinen and Erik Traneus, Ph.D. for guidance and the possibility to undertake research work in the field of radiotherapy physics.

I would like to express my gratitude to Emeritus Prof. Risto Johansson and Prof. Vesa Kataja from Kuopio University Hospital, Cancer Center for giving me the possibility to work in the department and for financial support. I am indebted to Adj. Prof. Anders Ahnesjö and Docent Simo Hyödynmaa for reviewing my thesis and providing valuable comments on the manuscript. I thank warmly Anssi Väänänen, Ph.D. from Kuopio University Hospital, Cancer Center for assistance with the BEAM treatment head model files and Ewen MacDonald for reading the English manuscript. I am also grateful to Jaakko Allinen for machining the eMLC collimator prototype.

I thank my wife Minna and our daughters Vilma and Miina for their love and support while writing the thesis.

Finally, I want to acknowledge the financial support from the Finnish Society of Oncology for their research grant, and Kuopio University Hospital (EVO-funding).

Joensuu April 21, 2011 *Tero Vatanen*

## ABBREVIATIONS

| | |
|---|---|
| CH | condensed electron history |
| CSD | collimator-to-surface distance |
| DVH | dose volume histogram |
| ECUT | cut-off energy for electrons |
| eIMRT | intensity modulated radiotherapy with electrons |
| eMLC | electron multi-leaf collimator |
| pMLC | photon multi-leaf collimator |
| MC | Monte Carlo |
| MERT | modulated electron therapy |
| MS | multiple scattering |
| PCUT | cut-off energy for photons |
| OAR | organ at risk |
| PTV | planning target volume |
| SSD | source-to-surface distance |
| VMC++ | Voxel Monte Carlo++ |

## SYMBOLS

| | |
|---|---|
| D5% | dose to 5% of the volume of interest from the DVH curve |
| $\Phi_D$ | direct electron fluence differential in energy and angle |
| $\Phi_I$ | indirect electron fluence differential in energy and angle |
| $ff$ | eMLC leaf front face surface |
| $\gamma$ | gamma index for the agreement between calculated and measured dose |
| $ie$ | eMLC leaf inner edge surface |
| $\kappa_{ff}$ | front face scatter kernel |
| $\kappa_{ie}$ | inner edge scatter kernel |
| $\Psi_B$ | bremsstrahlung photon energy fluence |

| | |
|---|---|
| $\mathrm{R}_{85}$ | therapeutic (85%) range |
| V20 Gy | percentage of the volume of interest with 20 Gy dose from the DVH curve |
| $z_{\mathrm{eff}}$ | distance to the virtual electron source |
| $\sigma$ | microscopic cross-section |
| $T$ | electron kinetic energy |
| $T_c, k_c$ | cut-off energies for electrons and photons which are explicitly followed in the MC simulation |
| $T, T'$ | incident and scattered electron kinetic energies |
| $k, k'$ | incident and scattered photon energies |
| $\left(\frac{\mathrm{d}T}{\rho \mathrm{d}x}\right)$ | mass stopping power |
| $L(E, T_c, k_c)$ | restricted stopping power for threshold energies $T_c$ and $k_c$ |
| $s$ | electron path |
| $\theta_s$ | multiple scattering angle |
| $\bar{s}$ | straight electron path length between the initial and final electron position in a condensed history step |
| $\psi$ | lateral deflection angle |
| $p_e$ | reduced momentum transfer |
| $F(\lambda, p_e)$ | MS distribution |
| $\varphi(E)$ | energy spectrum |
| $S, \tilde{S}$ | source and exit phase space planes |

## LIST OF PUBLICATIONS

This thesis is based on the following articles, which are referred in the text by their Roman numerals (I–IV):

I T. Vatanen, E. Traneus and T. Lahtinen. Dosimetric verification of a Monte Carlo electron beam model for an add-on eMLC. *Phys Med Biol*, 53:391–404, 2008.

II T. Vatanen, E. Traneus and T. Lahtinen. Comparison of conventional inserts and an add-on electron MLC for chest wall irradiation of left-sided breast cancer. *Acta Oncol*, 48:446–451, 2009.

III T. Vatanen, E. Traneus and T. Lahtinen. Enhancement of electron-beam surface dose with an electron multi-leaf collimator (eMLC): a feasibility study. *Phys Med Biol*, 54:2407–2419, 2009.

IV T. Vatanen, E. Traneus, A. Väänänen and T. Lahtinen. The effect of electron collimator leaf shape on the build-up dose in narrow electron MLC fields. *Phys Med Biol*, 54:7211–7226, 2009.

The original articles have been reproduced with permission from the copyright holders.

## AUTHOR'S CONTRIBUTION

The publications selected in this thesis are original research papers on multi-leaf collimation and Monte Carlo dose calculation of electron beams in radiotherapy. The author has done the simulations, measurements and data analysis related to publications **I-IV**. In Paper **IV**, modelling of the eMLC beam with BEAMnrc code was carried out by the author. Manuscripts for all papers have been written principally by the author with assistance from the co-authors.

# Contents

# 1 Introduction

## 1.1 ELECTRON BEAM RADIOTHERAPY

External electron beams are applied for radiotherapy of the skin or to targets near the skin surface. The types of electron beams in clinical use range from small fields with a size of a few centimetres to total skin irradiation of the patient. According to the International Commission on Radiation Units and Measurements (ICRU), the global use of electron beams varies from 10 to 15% of all cancer radiotherapy [95].

The relative biological effectiveness of megavoltage electron beams is approximately the same as can be attained with megavoltage photons [95]. However, depending on the beam energy, the surface dose of an electron beam is typically higher compared to a photon beam. With 16 MeV beam energy electrons, the surface dose is nearly 85%, which is approximately twice as high as obtained with a photon beam of the same nominal energy. The surface dose of electrons increases towards the higher electron beam energies. Often the surface dose is further increased with a water equivalent bolus material placed on the patient's skin [33,75,95,96,98]. Scattering materials in the electron beam, typically polymethylmethacrylate (PMMA), are used to increase the surface dose with total skin electron therapy and intraoperative radiotherapy [113].

Electrons are characterized by their limited range and their relatively uniform depth dose distribution near build-up maximum [73,95]. Hence, with beam energies between 4–20 MeV a high dose can be delivered to a depth of 1–7 cm. The electrons undergo millions of elastic and inelastic interactions with atoms while passing through the medium [55]. For example, an electron slowing down from 0.5 MeV to 1 keV will experience about $10^4$ collisions [7]. The energy loss of the electron increases towards the end of the electron's track [9]. However, due to the lateral scattering, the integrated dose from millions of electrons will lead to a depth dose curve that is a characteristic of electron beams i.e. a short dose build-up, plateau and a rapid dose fall-off. With small electron square field sizes, typically less than $5\times5$ cm$^2$, the depth of the dose maximum is shifted towards the phantom surface and the therapeutic range is reduced [95]. Actually, this effect depends on the nominal beam energy and is found for field sizes smaller than half of the electron range [39, 90]. An extended source-to-surface distance longer than 100 cm will lead to similar changes in the depth dose curve as seen with small fields.

Due to the limited range of electrons and rapid dose fall-off, the dose passing to the underlying healthy tissues is very low, usually only a few percent of the dose delivered to the target. This means that patient with a superficial target volume will likely suffer fewer adverse side effects compared to the situation with treatment by a megavoltage photon beam. Sometimes the best result is achieved with a combination of both electrons and photons. This is the case in the chest wall irradiation of breast cancer where matched adjacent electron and photon fields are applied.

Challenges encountered in the development electron beams are related to devising a more practical treatment delivery than the present technique of using low melting point-alloy inserts for beam collimation. On the other hand, beam modelling and dose calculation are complicated by the multiple scattering of electrons. The methods for increasing the surface dose with a bolus may not always be practical in clinical use due to complex patient anatomy and uncertainties in the positioning of the bolus. Additionally, the therapeutic range is reduced when applying scattering materials in the electron beam.

## 1.2 COLLIMATION OF ELECTRON BEAMS

Therapeutic electron beams with nominal energies from 4 to 50 MeV are produced by accelerating electrons to high velocities (comparable to the speed of light in a vacuum). The most common treatment units are scattering foil accelerators which can produce flattened beams in the energy range 4 to 20 MeV. Another type of treatment units is the scanning electron beam device which accelerates electrons via a microtron [42,47,85]. The term linear accelerator is commonly abbreviated as linac.

In conformal radiotherapy, a high dose is delivered to the target volume while sparing the healthy tissues and organs. Electron beams are shaped by primary collimators (e.g. jaws) and patient specific secondary electron collimators. Currently, secondary collimation according to target volume is usually based on the application of low melting point-alloy inserts or blocks. Inserts are made of different variations of Wood's metal, that is an alloy made from bismuth, lead, cadmium and tin with a melting point of approximately 70 °C. The Wood's metal has various trade names such as Cerrobend®. In an effort to avoid cadmium, Rose's alloy, such as MCP96® is used often instead of Wood's metal. The Rose's alloy has a melting point of 98 °C and it consist of bismuth, lead and tin. Patient specific inserts are made by casting.

Typically, electron inserts are mounted in a special applicator structure located at approximately 95 cm distance from the beam source. In an alternative method, a technique which uses several opposing, metallic leaves, called MLC, for electron beam shaping has been investigated [20,24,29,30,36,43–45,61,63,70,81,88,92,100]. Al-Yahya et al. have proposed a slightly different approach for secondary collimation with the so-called few-leaf electron collimator [2, 4]. Collimation based on the existing photon MLC (also known as pMLC) has also been investigated. Although the initial results of utilizing a pMLC for electron beam collimation described by Klein et al. [61] were not very encouraging, this option has been further studied [24, 45, 46, 63, 64, 70, 88]. Problems with using the pMLC with electron beams are related to the need for a longer collimator-to-surface distance than with eMLC, which causes increased electron scatter in air. Klein et al. have reported penumbras from 13 to 29 mm for SSD between 70 and 80 cm [61]. With inserts they found markedly smaller penumbras between 10 and 12 mm which is similar to the penumbra for an eMLC beam at

SSD 100 cm [70]. As a special case with scanning electron beam accelerators, the pMLC has been found to be suitable for electron beam collimation with a 12 mm penumbra for 10 MeV energy at SSD 100 cm [42, 43, 46, 88, 122].

Both eMLC leaf thickness and the material influence the amount of leaf transmitted dose and also the energy and fluence distribution of electrons scattered from leaves. The existing eMLC prototypes consists of 2.54 cm thick steel leaves [81], 1.8 cm and 3.0 cm thick brass leaves [30, 36], and 1.6 cm thick leaves made of a low melting point alloy [100]. Leaves made of steel result in higher transmission of treatment head generated bremsstrahlung photons and a slightly wider fluence distribution compared to tungsten leaves [81].

For large field sizes, similar eMLC beam profiles for leaves focussed on the source and straight leaf ends have been reported [70]. With electron beams collimated by a pMLC, there appears to be a negligible difference between round and leaves focussed on the source [44]. Compared with straight pMLC leaves, round pMLC leaf ends have been reported to yield slightly more uniform dose profiles [81].

For a standard electron applicator and an insert as a secondary collimator the treatment is typically delivered at a fixed SSD due to the short collimator-to-surface distance. Tenhunen et al. have reported an isocentric technique with short applicators [110]. For eMLC prototypes, the standard electron applicator of the linac has been redesigned [81,100] or removed in the installation of the eMLC [29, 36]. In the latter case, both fixed SSD and isocentric electron irradiations became possible [29,30,36].

An eMLC might offer a more advanced and less laborious collimation than electron inserts. With an eMLC it would also be possible to produce intensity modulated electron beams. A simple example of electron beam modulation is the combination of adjacent electron beams with different energies and weights [46,60,122]. Depth dose can be modulated by summing fields with different energies and weights [38,94]. However, the present treatment units do not have devices that could produce intensity modulated electron beams. Archambeau et al. [8] and Low et al. [75,76] have developed range modulation techniques with water-equivalent bolus materials or compensators that are individually machined for each patient and placed on the skin [67,98]. Advanced techniques that are based on modulating the actual beam with a collimator, such as intensity modulated radiotherapy with electrons (eIMRT) or modulated electron therapy (MERT) are under research [3,20,23,69,78,81,94,124].

## 1.3 BEAM MODELLING

If one wishes to perform Monte Carlo (MC) dose calculations in a patient, one must have information on the fluence, energy and angle distribution of incident particles, photons, electrons and positrons, from the linear accelerator. This information is usually calculated in a exit phase space that is underneath all beam modifying devices or collimators. There are two basic ways for doing the calculation of the exit phase space. A full treatment head MC simulation of the linear accelerator requires that one is aware of the treatment head geometry, as well as the materials and energy and angle distributions of the electron source. However, usually this data is not reported accurately. The second option is to use a semi-empirical beam model which is based on different sources of electrons and photons in the treatment head. Structures and collimators in the electron beam, such as the eMLC, contribute to the dose component from collimator scattered particles and have to be included in the beam model. This kind of beam model offers better than 2% accuracy and achieves a faster exit phase space reconstruction (by a factor of 10) than with a full treatment head simulation [41,82].

Semi-empirical methods are needed to match the simulated and real accelerator beams as accurately as possible. In beam modelling this refers to a process called beam characterization where the beam model parameters are changed iteratively. Usually the energy distribution of source electrons is adjusted until the calculated and measured depth dose curves agree. Subsequently, the model parameters related to lateral electron distribution are varied until there is a good agreement in the field profiles. Typically, the beam characterization measurements are conducted in a simple geometry, such as in a homogenous water phantom, where it is possible to calculate dose accurately.

## 1.4 DOSE CALCULATION

Since there is a steep dose response of tumors and healthy tissues, it is important to develop calculation methods and treatment techniques to achieve accurate delivery of the dose to the target volume [15]. Electrons interact primarily with matter via inelastic scattering (electron-electron scattering), bremsstrahlung and elastic scattering [10,89]. Simultaneously, primary and secondary photons interact via a photoelectric effect, Compton and coherent scattering, and pair production. These processes produce new charged particles in the form of photoelectrons, Compton electrons, and electron–positron pairs. Electrons and positrons lose energy to the medium through many collisions with atoms and electrons. These collisions can be divided into (1) ionizational (also known as collisional) losses and (2) radiative losses (bremsstrahlung production). The electrons released in the ionizational collisions are generally of low energy and release their energy locally [89]. In hard collisions, the scattered electron has enough energy to travel away from its point of origin and to trigger further ionization. These electrons are called delta rays. The energy of bremsstrahlung photons is nearly uniformly distributed between zero and the electron energy [89]. In human tissues at lower energies, ionizational losses are more probable and at very high energies (over 100 MeV) radiative losses predominate [9, 12]. In addition to the energy losses in inelastic collisions, electrons and positrons interact by particle–antiparticle annihilation, producing a pair of annihilation photons [89]. The gradual energy loss of particles by multiple scattering means that the solution of the transport problem is highly dependent on its boundary conditions [89]. It is possible to solve the Boltzmann transport equation for electron beams by a finite element method, although the calculation is time-consuming [14].

Clinical electron beam planning has been traditionally based on semi-empirical dose calculation algorithms and pencil beam models [16,37]. The generalized Gaussian pencil beam model takes into account large angle single scattering and range straggling [16]. In these models the energy deposition from beam particles, photons, electrons and positrons is typically modelled in a homogenous and semi-infinite water phantom. The dose in the patient is then calculated by summing many pencil beams in the medium with the actual electron densities of the different tissues. However, in a heterogenous tissue, the estimate of the lateral energy deposition from a pencil beam may not be correct due to the intense elastic and inelastic scattering of electrons. This can lead to a reduced (over 5%) accuracy in the dose calculation [106]. Larger deviations may be found near to the interfaces of tissues with high and low densities such as bone and lung or air cavities [21,22,55].

The Monte Carlo method uses repeated sampling of known interaction probability distributions to simulate the tracks of photons, electrons and positrons [57]. Large numbers of electrons (millions) have to be simulated in order to obtain a statistically meaningful dose distribution. The traditional MC algorithms, such as BEAMnrc code system [103, 120], require computational resources and time from tens of minutes up to hours. If it is to be feasible in clinical treatment planning, it must be possible to calculate patient dose distribution in a few minutes. In the VMC++ algorithm developed by Kawrakow et al. [48,50,52,55] this is realized mainly by reducing "separate" electron histories, by neglecting explicit simulation of bremsstrahlung photons and making approximations of the bremsstrahlung and inelastic scattering cross-sections. These simplifications are known to have only a minor effect (2%) on the accuracy of the calculated dose [50,55]. Therefore, in this work the VMC++ algorithm was applied for dose calculation of the eMLC beam.

# 2 Aims of the thesis

The main goals of this thesis were

- to study the feasibility of using a new eMLC as an add-on device for use with an existing electron applicator of the linear accelerator.
- to apply MC based modelling and dose calculation for the eMLC beam.
- to examine small and narrow eMLC fields as a choice for the bolus technique to increase electron beam build-up dose.
- to investigate the effect of eMLC leaf geometry on build-up dose of the add-on electron MLC.

# 3 Monte Carlo simulation of megavoltage electron beams

## 3.1 MONTE CARLO METHOD

The Monte Carlo method uses known interaction probability distributions and repeated sampling of random numbers to simulate tracks of particles, namely photons, electrons and positrons [89, 101]. This involves the calculation of particles energy, charge, position and direction, which is also known as the determination of the phase space. In the simulation of megavoltage electrons, one needs to model the beam and dose to be delivered to the patient (figure 3.1).

In each step of the simulation, a sample $x^*$ of a random variable with a probabiliy density function $f(x)$ and cumulative distribution $F(x)$ is selected. The principle of sampling is as follows. Select a uniformly distributed random number $r^*$ from the unit interval $[0, 1]$ such that

$$r^* = F(x^*) = \int_{-\infty}^{x^*} f(x)\mathrm{d}x. \tag{3.1}$$

The quantity of interest (interaction type, scattering angle, etc.) is calculated by inversion, or direct sampling, as

$$x^* = F^{-1}(r^*). \tag{3.2}$$

Another common method is rejection sampling [89]:

1. Generate two random numbers $\{r_1^*, r_2^*\} \in [0, 1]$.
2. Calculate $x^* = a + (b - a)r_1^*$
3. Accecpt $x^*$, if $r_2^* \leq \frac{f(x^*)}{M}$, $\quad M = \mathrm{Sup}_{x \in [a,b]} f(x)$. If not, go to step 1.

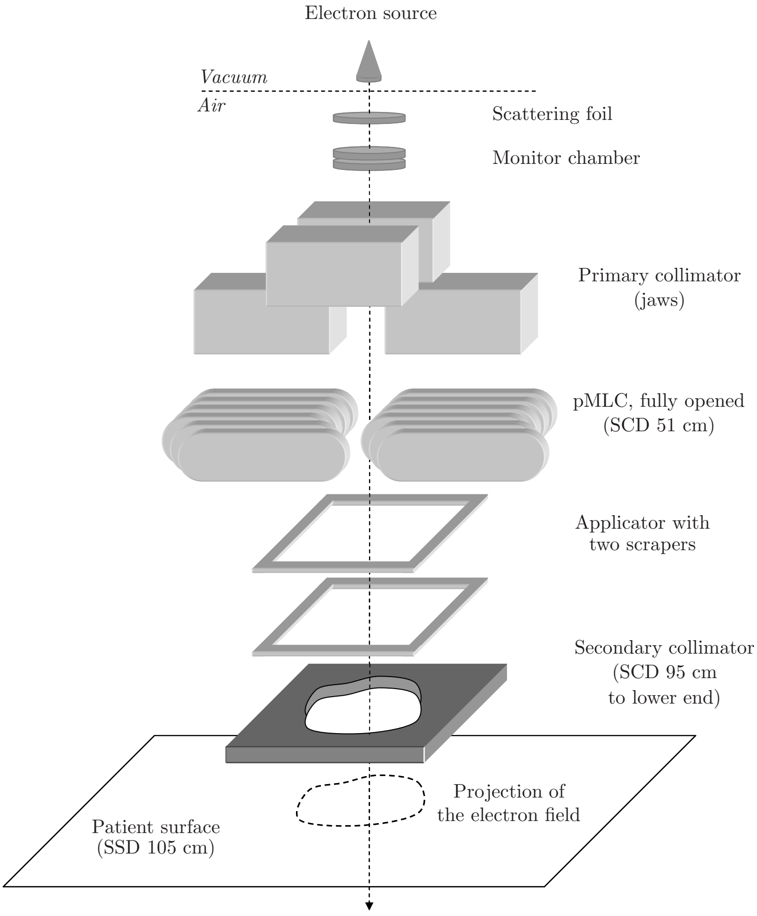

*Figure 3.1: Typical electron beam collimation from a linear accelerator. The figure shows the main collimators and beam modifying devices including the low melting point-alloy insert (dark grey color). Not shown are the mirror (below the monitor chamber) and acrylic foil (below pMLC) for the light field and graticule.*

The transport equation for electrons is

$$\frac{\mathrm{d}\Phi(\mathbf{x},\Omega,E,t)}{\mathrm{d}t} = S_e(\mathbf{x},\Omega,E,t) + vI[\Phi], \tag{3.3}$$

where $\Phi(\mathbf{x},\Omega,E,t)$ is the electron fluence, $S(\mathbf{x},\Omega,E,t)$ the number of electrons with energy $E$ and velocity $\mathbf{v} = (v,\Omega)$ at a position $\mathbf{x}$ per unit volume, energy and solid angle interval, imparted per unit time by an external source or by photons interacting with the medium at time $t$ [57,89]. The coupling of the electron and photon fluences is included in the source term. The total time derivative is

$$\frac{\mathrm{d}\Phi(\mathbf{x},\Omega,E,t)}{\mathrm{d}t} = \frac{\partial\Phi(\mathbf{x},\Omega,E,t)}{\partial t} + v\nabla\Phi(\mathbf{x},\Omega,E,t). \tag{3.4}$$

The changes of the particle fluence due to collisions with atoms or molecules $n(\mathbf{x})$ are given by the collision term

$$\begin{aligned} I(\Phi) = &-n(\mathbf{x})\Phi(\mathbf{x},\Omega,E,t)\int_0^E \mathrm{d}E' \int_{4\pi} \mathrm{d}\Omega'\sigma(E,E',\Omega',\mathbf{x}) \\ &+n(\mathbf{x})\int_E^\infty \mathrm{d}E' \int_{4\pi} \mathrm{d}\Omega'\Phi(\mathbf{x},\Omega,E',t)\sigma(E,E'-E,\Omega'\cdot\Omega,\mathbf{x}), \end{aligned} \tag{3.5}$$

where $\sigma(E,E'-E,\Omega'\cdot\Omega,\mathbf{x})$ is the microscopic cross-section at a position $\mathbf{x}$ for all interactions in which an electron with energy $E$ loses energy $E-E'$ and scatters to angle $\Omega$.

The collision integral $I(\Phi)$ represents the balance between particle losses and gains due to interactions described by the cross-section $\sigma(E,E'-E,\Omega,\mathbf{x})$. Equation 3.3 is solved formally in a Monte Carlo simulation by

$$\Phi(\mathbf{x},\Omega,E,t) = \int_0^t \mathrm{d}t_0 \int_E^\infty \mathrm{d}E_0 \int \mathrm{d}\mathbf{x}_0 \int_{4\pi} \mathrm{d}\Omega_0 S_e(\mathbf{x}_0,\Omega_0,E_0,t_0)\Phi_0, \tag{3.6}$$

where $\Phi_0(\mathbf{x},\Omega,E,t) := \Phi_0(\mathbf{x}_0,\Omega_0,E_0,t_0;\mathbf{x},\Omega,E,t)$ is the solution of 3.3 for a source $S_{e,0}$ i.e. a single particle from the source set in motion at time $t_0$ with energy $E_0$ and direction $\Omega_0$ at a position $\mathbf{x}_0$ [57].

## 3.2 INTERACTIONS AND CROSS-SECTIONS

The most important electron interactions are inelastic electron–electron scattering, bremsstrahlung interaction and elastic scattering, which are based on electromagnetic forces between atoms and particles. The total microscopic cross-section $\sigma$ for electrons is the sum of the microscopic cross-section for inelastic collisions with atomic electrons, $\sigma_{\text{inel}}$, the microscopic bremsstrahlung cross-section $\sigma_{\text{brem}}$, and the microscopic elastic scattering cross-section $\sigma_{\mathrm{el}}$:

$$\sigma(E,E',\Omega,\mathbf{x}) = \sigma_{\mathrm{inel}}(E,E',\Omega,\mathbf{x}) + \sigma_{\mathrm{brem}}(E,E',\Omega,\mathbf{x}) + \sigma_{\mathrm{el}}(E,E',\Omega,\mathbf{x}), \tag{3.7}$$

where $\mathbf{x} = (x,y,z) \in \mathbb{R}^3$. The macroscopic cross-section is

$$\Sigma(E,E',\Omega,\mathbf{x}) = n(\mathbf{x})\sigma(E,E',\Omega,\mathbf{x}). \tag{3.8}$$

Integration of the macroscopic cross-section over $E'$ and $\Omega'$ gives the number of interactions per unit length for electrons with energy $E$. The atom or molecule density $n$ is

$$n = \rho \frac{N_A}{M_A} \tag{3.9}$$

where $N_A = 6.022045 \cdot 10^{23}$ mol$^{-1}$ is the Avogadro's constant, $M_A$ the molar mass in mol$^{-1}$.

### 3.2.1 Stopping power

Electrons lose energy to the medium through collisions with the electrons in the medium, resulting in ionization and exitations of the atoms. These collisions are divided into soft and hard collisions. Soft collisions produce energy transfers less than a cut-off value $\Delta$, and deposit energy locally, while hard collisions produce energy transfers greater than $\Delta$, resulting in knock-on electrons or delta rays which can produce ionization tracks. On the whole, hard collisions are rare events but have a large energy transfer [89].

Stopping power $\frac{\mathrm{d}T}{\mathrm{dx}}$ is the average energy loss per unit path length for electrons including both hard and soft collisions. The stopping power divided by the density of the material is called the mass stopping power (in units of MeVcm$^2$g$^{-1}$, figure 3.2)

$$\left(\frac{\mathrm{d}T}{\rho \mathrm{d}x}\right) = \frac{2\pi N_A r_0^2 m_0 c^2}{\beta^2}\frac{Z}{A}\left[\ln\frac{T^2(T+2)}{2\left(\frac{I}{m_0c^2}\right)^2} + \frac{T^2/8-(2T+1)\ln 2}{(T+1)^2} + 1 - \beta^2 - \delta\right] \tag{3.10}$$

where $T$ is the kinetic energy of the electron (in units of $m_0c^2$), $\beta = v/c$, $I$ is the mean ionizational potential in MeV and $\delta$ is the density effect correction factor [89].

The restricted stopping power $\left(\frac{\mathrm{d}T}{\rho \mathrm{d}x}\right)_\Delta$ includes only soft collisions with energy transfer less than $\Delta$. $L(E, T_c, k_c)$ is the restricted stopping power for threshold energies $T_c$ and $k_c$,

$$\begin{aligned} L(E, T_c, k_c) &= L_{\text{coll}}(E, T_c) + L_{\text{rad}}(E, k_c) &\quad (3.11)\\ L_{\text{coll}}(E, T_c) &= \int_0^{T_c} \mathrm{d}E' \Sigma_{\text{inel}}(E, E')E' &\quad (3.12)\\ L_{\text{rad}}(E, k_c) &= \int_0^{k_c} \mathrm{d}E' \Sigma_{\text{brem}}(E, E')E'. &\quad (3.13) \end{aligned}$$

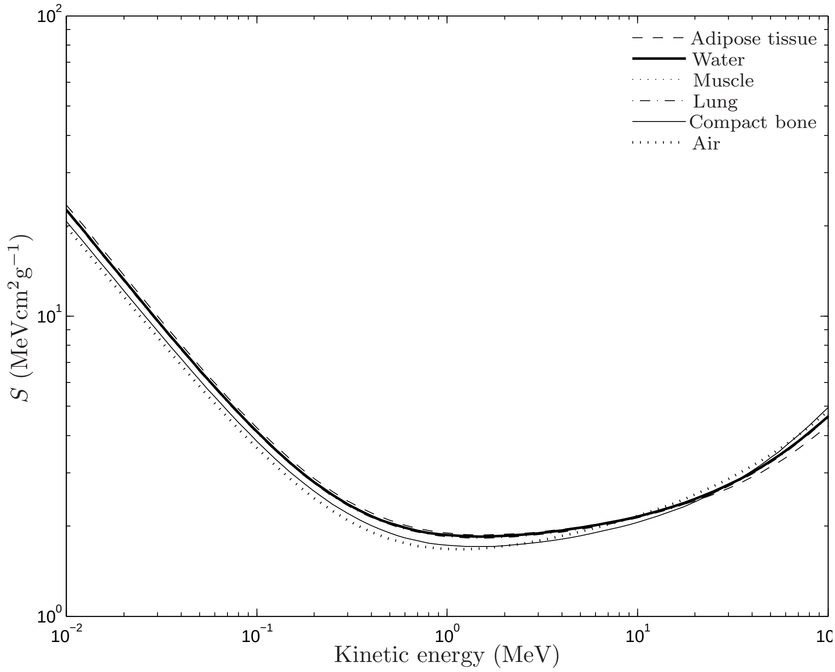

*Figure 3.2: Mass stopping power as a function of electron energy for different biological materials and air on a logarithmic scale [12].*

### 3.2.2 Inelastic scattering

The Møller cross-section for the inelastic electron–electron scattering differential in the kinetic energy $T'$ of the scattered electron is [57]

$$\frac{d\sigma^{-}_{\mathrm{inel}}}{dT'} = \frac{2\pi r_0^2 m}{\beta^2}\frac{1}{T'^2}\left[1 + \frac{T'^2}{(T-T')^2} + \frac{\tau^2}{(\tau+1)^2}\left(\frac{T'}{T}\right)^2 - \frac{2\tau+1}{(\tau+1)^2}\frac{T'}{(T-T')}\right] \tag{3.14}$$

where $\beta$ is the incident electron velocity in units of the speed of light, $T$ the incident kinetic energy in units of $m_0c^2$ and $\tau = T/m$. The scattered electron is assumed to be initially at rest. By definition, the electron with the higher energy after the collision is considered to be the primary electron. Let $aT$ be the kinetic energy of the secondary electron. The polar scattering angle $\theta$ of the primary electron can be calculated from [89]

$$\cos\theta = \left[\frac{(1-a)(T+2)}{(1-a)T+2}\right]^{1/2}, \quad 0 \le a \le \frac{1}{2} \tag{3.15}$$

and the scattering angle $\theta'$ of the secondary electron from

$$\cos\theta' = \left[\frac{a(T+2)}{aT+2}\right]^{1/2}. \tag{3.16}$$

When most of the energy is left to the primary electron, the scattering is at forward angles [105].

The total cross-section for Møller interactions is obtained via integration of 3.14 from $T_c$ to $T/2$:

$$\sigma^{-}_{\mathrm{inel}} = \int_{T_c}^{T/2} \frac{d\sigma^{-}_{\mathrm{inel}}}{dT'} dT' \tag{3.17}$$

The Bhabha cross-section is the cross-section for the positron–electron scattering differential in the kinetic energy of the scattered electron which is initially at rest. The Bhabha cros section also depends mostly on the incident particle's kinetic energy [57].

### 3.2.3 Bremsstrahlung

The bremsstrahlung cross-section for an electron with a total energy $E$ incident on an atom with atomic number $Z$, differential in the photon energy $k$, is calculated by First Born approximation Bethe-Heitler cross-sections with an empirical correction factor $A'(E,Z)$:

$$\frac{\mathrm{d}\sigma_{\mathrm{brem}}(E,Z)}{\mathrm{d}k} = \frac{A'(E,Z)r_0^2\alpha Z(Z+\xi(Z))}{k}\left[\left(1+\frac{E'^2}{E^2}\right)\right.$$
$$\left.\left(\phi_1(\delta)-\frac{4}{3}\ln Z\right)-\frac{2}{3}\frac{E'}{E}\left(\phi_2(\delta)-\frac{4}{3}\ln Z\right)\right] \tag{3.18}$$

where $E' = E - k$ is the electron energy after the interaction, $r_0 = 2.81794 \cdot 10^{-15}$ m the classical electron radius, $\alpha$ the fine structure constant and

$$\delta = 136Z^{-1/3}\frac{km}{EE'}. \tag{3.19}$$

The functions $\phi_1(\delta)$, $\phi_2(\delta)$ are called mass screening correction parameters and $\xi(Z) = L'_{\mathrm{rad}}(Z)/L_{\mathrm{rad}}(Z)$ [57]. The bremsstrahlung photons are emitted at forward angles [105] and the interaction happens near to the nucleus [9]. Therefore, bremsstrahlung is more likely in a high-$Z$ materials and the cross-section depends on $Z^2$.

### 3.2.4 Elastic scattering

The screened Rutherford cross-section, differential in the cosine $\mu$ of the polar scattering angle of electrons or positrons incident on atoms of atomic number $Z$, is

$$\frac{\mathrm{d}\sigma_{sr}}{\mathrm{d}\mu} = \frac{2\pi r_0^2 Z^2}{\beta^2\tau(\tau+2)}\frac{1}{(1-\mu+2\eta)^2} \tag{3.20}$$

where $\beta$ is the particle velocity in units of the speed of light, $\tau$ the kinetic energy $T$ in units of $m$ and $\eta$ the screening parameter [57]. By integrating 3.20 over $\mu$ from -1 to 1, the total elastic scattering cross-section is calculated as

$$\sigma_{SR} = \frac{\pi r_0^2 Z^2}{\beta^2\tau(\tau+2)\eta(1+\eta)}. \tag{3.21}$$

Backscattering may happen mostly in materials with a high atomic number and with low electron kinetic energies [9].

### 3.2.5 Photon interactions

In the radiotherapy energy range 4-20 MeV, the main photon interactions are well known, i.e. photoelectric effect, Compton and coherent scattering, and pair production process. The Klein-Nishina cross-section for the Compton scattering differential of the cosine for the polar angle of the scattered photon with respect to the initial direction is

$$\frac{\mathrm{d}\sigma_{\mathrm{kn}}}{\mathrm{d}\cos\theta} = \pi r_0^2 Z \left(\frac{k'}{k}\right)^2 \left[\frac{k'}{k} + \frac{k}{k'} - \sin^2\theta\right] \tag{3.22}$$

where $k' = \frac{E'}{m_0 c^2}$ is the energy of a photon scattered at an angle $\theta$ [57]. In the above equation, the electron is assumed to be free and initially at rest. The energy of the scattered photon is related to incident photon energy $k = \frac{E}{m_0 c^2}$ and photon scattering angle $\theta$ by the kinematics of the collision:

$$k' = \frac{k}{(1 + k(1 - \cos\theta))}. \tag{3.23}$$

## 3.3 ELECTRON TRANSPORT

### 3.3.1 Multiple scattering

Since electrons undergo a large number of interactions in a short distance, it is not practical to model every scattering event. Instead, the electrons are transported in a schematized random walk, in which each step or path increment accounts for the effects of a multitude of collisions [49, 89]. This modelling is also known as the condensed history approximation [7, 57]. The energy loss between hard collisions and bremsstrahlung interactions is calculated as a continuous energy loss, whereas the change in direction due to elastic scattering is modelled by the multiple scattering distribution.

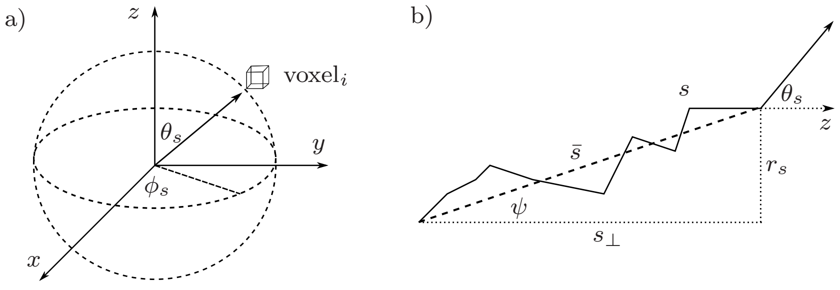

*Figure 3.3: a) Spherical coordinate system. b) Electron path s, the multiple scattering angle $\theta_s$, the lateral deflection angle during the step $\psi$ and the straight line distance between initial and final position $\bar{s}$ (modified from [50]). Ideally, the calculated electron path should converge to the true electron path, when $\bar{s}$ approaches zero.*

The path-length $s$ satisfies $\mathrm{d}s/\mathrm{d}t = v$ and

$$\frac{\mathrm{d}E}{\mathrm{d}s} = -L(E, E_c, k_c), \quad s = \int_E^{E_0} \frac{\mathrm{d}E'}{L(E, E', k_c)}. \tag{3.24}$$

The approximation 3.24 is known as the continuous slowing down approximation (CSDA).

Assume that the lateral deflections during the step are neglected, i.e. the angle $\psi$ is zero. The direction cosines with respect to $x$, $y$ and $z$ axis at the beginning of the step are $(u_x, u_y, u_z)$. Let the polar axis of spherical coordinate system be along the direction of motion of the electron ($w = 1$) and $\theta_s$ and $\phi_s$ the polar and azimuthal angles of scattering (figure 3.3). The new direction cosines at the end of the step are then

$$\begin{aligned} u'_x &= \cos\phi_s \sin\theta_s \\ u'_y &= \sin\phi_s \sin\theta_s \\ u'_z &= \cos\theta_s. \end{aligned} \tag{3.25}$$

In the case when the electron's initial motion is not along $z$-axis ($u_x \neq 1$, $u_y \neq 1$ and $u_z \neq 1$), the new direction cosines are [89]

$$u'_x = u_x \cos\theta_s + \frac{u_x u_z \sin\theta_s \cos\phi_s - u_y \sin\theta_s \sin\phi_s}{\sqrt{1 - u_z^2}}$$

$$u'_y = u_y \cos\theta_s + \frac{u_y u_z \sin\theta_s \cos\phi_s + u_x \sin\theta_s \sin\phi_s}{\sqrt{1-u_z^2}}$$
$$u'_z = u_z \cos\theta_s - \sin\theta_s \cos\phi_s \sqrt{1-u_z^2}. \tag{3.26}$$

The azimuthal angle $\phi_s$ is uniformly distributed between $[0, 2\pi]$ and $\theta_s$ is sampled from a multiple scattering distribution. A simple choice is the Gaussian distribution

$$p(\theta_s)\mathrm{d}\theta_s = \frac{2}{\bar{\theta}^2} \exp\left(-\frac{\theta_s^2}{\bar{\theta}^2}\right) \mathrm{d}\theta_s, \tag{3.27}$$

where $\bar{\theta}^2$ is the mean square scattering angle [89]. Multiple scattering distributions that better account for large angle deflections have been developed e.g. by Goudsmit and Saunderson [32].

### 3.3.2 Path length correction

The CSDA approximation gives a mean energy loss per unit path length. In reality, there is a statistical distribution for electron energy loss, called the energy loss straggling distribution which results from stochastic variations in rates of energy loss [9, 89]. Starting from momentum transfer and the screened Rutherford cross-section, Kawrakow [49] has derived a MS distribution

$$F(\lambda, p_e) = \frac{2}{p_{e,0}^2}(1-\eta_1-\eta_2)\exp\left(-\frac{p_e^2}{p_{e,0}^2}\right) + \frac{2\mu_1^2\eta_1}{(p_e^2+\mu_1^2)^2} + \frac{4\mu_2^2\eta_2}{(p_e^2+\mu_2^2)^3}, \tag{3.28}$$

where $p_{e,0}, \mu_1, \mu_2, \eta_1$ and $\eta_2$ are parameters which depend on $\lambda$, the average number of elastic collisions per step:

$$\lambda = \frac{b_c s}{\beta^2}. \tag{3.29}$$

The $\beta$ is the electron's velocity (in units of $c$). In 3.28, the $p_e$ is the so-called reduced momentum transfer and $\lambda$ is a material specific quantity. The scattering angle $\theta_s$ is related to $y$ as [50]

$$\cos\theta_s = 1 - \frac{\chi_{cc}^2 s}{2E^2\beta^4} p_e^2. \tag{3.30}$$

The energy dependent parameters $b_c$ and $\chi_{cc}$ describe the scattering properties of the medium according to the theory of Molière [48]. In Kawrakow's model the lateral deflections during the step are included in the calculation of the final position of the electron and path length $\bar{s}$. Since the distribution of number of collisions is Poissonian, the final position of electron can be calculated as [48] (electron's motion prior to scattering is along the $z$-axis)

$$\begin{aligned} x &= \bar{s}\sin\psi\cos(\phi_s + \tilde{\phi}) \\ y &= \bar{s}\sin\psi\sin(\phi_s + \tilde{\phi}) \\ z &= \bar{s}\cos\psi. \end{aligned} \tag{3.31}$$

The angle $\tilde{\phi}$ is sampled from an actual distribution [48]. The straight line path is given by

$$\bar{s}^2 = \frac{2s^2}{\xi}\left(1 - \frac{1-e^{-\xi}}{\xi}\right), \quad \xi = \frac{1}{2}T_s s. \tag{3.32}$$

The scattering power $T_s$ is

$$T_s = \frac{2b_c^2}{\beta^2}(1 - \langle\cos\Theta\rangle), \tag{3.33}$$

where $\langle\cos\Theta\rangle$ is the average polar scattering angle in a single electron scattering [50]. The lateral deflection angle $\psi$ is related to the scattering angle $\theta_s$ as

$$\cos\psi = 1 - \alpha(1 - \cos\theta_s) \tag{3.34}$$

together with

$$\alpha \approx \frac{1}{3}\left(1 + \frac{\xi}{4} + \frac{\xi^2}{360} - \frac{19\xi^3}{4320}\dots\right). \tag{3.35}$$

The electron's position according 3.31 and the above equations is valid when the energy loss during the step is neglegted. The path length correction in both lateral ($\psi$) and longitudinal directions ($z$) is accordingly [48]:

$$\alpha = \alpha_{1/2}(1 - \epsilon/4) \tag{3.36}$$

$$\bar{s} = \bar{s}_{1/2}\frac{1 - \alpha_{1/2}(1 - \exp -\xi)}{1 - \alpha_{1/2}(1 - \exp(-\xi))(1 - \epsilon/4)}, \tag{3.37}$$

where $\epsilon$ is the parameter for energy loss fraction per step (usually set to 0.25) and $\bar{s}_{1/2}$ the path length during which the electron loses half of its kinetic energy. Since the average electron energy during the step $E_{1/2}$ is used to sample the MS scattering angle, there is a limit to the maximum allowable step length

$$\bar{s}_{\mathrm{max}} = \min\left(\frac{1}{T_s}, \bar{s}_{1/2}\right). \tag{3.38}$$

With 10 and 0.1 MeV electron energies, the $\bar{s}_{\mathrm{max}}$ values are approximately 1.0 and 0.01 cm [48].

# 4 The VMC++ algorithm

VMC++ algorithm is optimized for three dimensional dose calculations in voxels defined by computer tomography images of the patient [48,50,52,55]. The principal concept is that it involves some approximations which make the simulation quick to perform (within minutes).

## 4.1 INELASTIC SCATTERING

The Møller cross-section 3.14 is a function of the kinetic energies of the electron $T$ and delta particle $T'$,

$$\frac{\mathrm{d}\sigma_\delta(T,T')}{\mathrm{d}T'} = \frac{f(T,T')}{T'^2}. \tag{4.1}$$

Since $f(T,T')$ varies slowly with $T'$, the production of secondary electrons is sampled from an approximate $\frac{1}{T'^2}$ distribution [55].

## 4.2 BREMSSTRAHLUNG

The differential cross-section for bremsstrahlung 3.18 is a function of the incident electron energy $E$ and bremsstrahlung photon $k$

$$\frac{\mathrm{d}\sigma_\gamma}{\mathrm{d}k} = \frac{g(E,k)}{k} \tag{4.2}$$

where $g(E,k)$ is a complicated function of $E$ and $k$. However, $g$ depends only slightly on $k$. Hence, only the $1/k$ dependence is taken into account for the differential cross-section [55]. Bremsstrahlung photons are not simulated. Instead, the dose from bremsstrahlung photons in the phantom and from the linac treatment head is added from a measured dose profile in water. Therefore, bremsstrahlung that is produced in the patient is not modelled explicitly.

## 4.3 NUMBER OF PARTICLE HISTORIES

Assume that there are two electron sources emitting "separate" electrons i.e. in a certain voxel there is a dose contribution from electrons from only one of the two sources. In this case, a simulation with $N/2$ electrons from two adjacent sources is equivalent to simulation from a single source with $N$ electrons. In the VMC++ model, a single electron history is applied $N_r$ times in the phantom. The total number of histories is $N = N_r N_h$, where $N_h$ is the number of different histories. Simulations with $N_r \leq 4 \text{ cm}^{-2}$ (and $N_h = 5 \cdot 10^4$) are possible without impairing unfavourably on the statistical uncertainty of the dose [55].

## 4.4 ENERGY DEPOSITION

### 4.4.1 In water

The electron's history is formed by a series of steps $s_1, s_2, \ldots, s_i$ until a cut-off energy is reached. Before each step with initial energy $E_i$ the path $s_i$ to the next discrete interaction is sampled from the probability distribution

$$F(\hat{x}) = \exp(-\hat{x}), \quad \hat{x} = \int_0^s (\Sigma_\delta(E_i, s') + \Sigma_\gamma(E_i, s')\mathrm{d}s', \tag{4.3}$$

where $\Sigma_\gamma$ and $\Sigma_\delta$ are the macroscopic bremsstrahlung and Møller cross-sections. If $t_i \geq t_{\max}$, no secondary particle is produced and the new electron energy is

$$E_{i+1} = E_i - \Delta E_{i,\gamma} - \Delta E_{i,\delta}. \tag{4.4}$$

In this step, the deposited energy is $\Delta E_{i,\delta}$ since the bremsstrahlung photons are omitted from the simulation (section 4.2). When $s_i < s_{\max}$, the probability for a delta particle production is $\Sigma_\delta/(\Sigma_\delta + \Sigma_\gamma)$. A photon is emitted with probability $\Sigma_\gamma/(\Sigma_\delta + \Sigma_\gamma)$. The energy of secondary particles is selected from the respective approximated differential cross-sections 4.1 and 4.2.

Based on the CSDA approximation, the energy is deposited in a small volume element, or voxel, corresponding to the straight path length in the voxel:

$$\Delta E_1(\text{this voxel}) = \Delta E_1 \frac{\Delta s_1(\text{this voxel})}{s_1}. \tag{4.5}$$

If no voxel boundaries are crossed (figure 4.1), the total energy is left in the current voxel [55]. The new direction of the electron is calculated from the MS angle distribution 3.28.

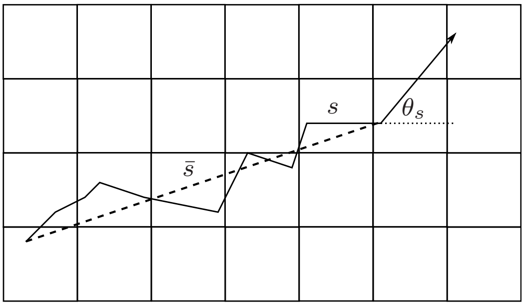

*Figure 4.1: Illustration of an electron path s and scattering angle $\theta_s$ in a geometry defined by three-dimensional rectilinear voxels. Only a two-dimensional plane is shown.*

### 4.4.2 In heterogeneous tissue

In a heterogeneous tissue, the total energy loss must be equal to the energy loss in water. Hence, the electron's path length $s$ in the voxel has to be scaled with the stopping power of the medium, $(\mathrm{d}T/\mathrm{d}x)$:

$$s = s_0 \frac{(\mathrm{d}T/\mathrm{d}x)_0}{(\mathrm{d}T/\mathrm{d}x)} \tag{4.6}$$

where $s_0$ and $(\mathrm{d}T/\mathrm{d}x)_0$ are the path length and stopping power in water, respectively. Similarly, the average number of elastic collisions in the actual medium $\lambda$ is determined from the value of water, $\lambda_0$:

$$\lambda = \frac{b_c s}{\beta^2} = \lambda_0 \frac{b_c (\mathrm{d}T/\mathrm{d}x)_0}{b_{c,0}(\mathrm{d}T/\mathrm{d}x)} = \lambda_0 f_\lambda. \tag{4.7}$$

Equation 3.34 relates to the reduced momentum transfer $p_e$ and scattering angle $\theta_0$ in water and is re-written as

$$\begin{aligned}\cos\theta &= 1 - \frac{\chi_{cc}^2 S_0}{\chi_{cc,0}^2}(1-\cos\theta_0) \\ &= 1 - f_\chi(1-\cos\theta),\end{aligned} \tag{4.8}$$

where the scattering angle in the medium s denoted with $\theta$. Hence, there are two tissue-specific parameters, $f_\lambda$ and $f_\chi$, which are determined from computer tomography images by fitting a calibration curve for the mass density against the Houndsfield number [50,55].

The electron transport theory of section 3.3.2 provides information on the probability distribution of finding an electron at a certain position after travelling a path length $s$. However, the electron's trajectory between the initial and final position is not known. So, the exact position where the voxel boundaries are crossed cannot be determined. Therefore, the following approximations are needed [50]:

1. Transport the electron on a straight line between the initial and final position i.e. approximate $s$ with $\bar{s}$.
2. Instead on $\lambda$ of the actual medium, use the number of elastic collisions of water $\lambda_0$.
3. When crossing a voxel boundary, calculate the lateral deflection angle $\psi$ from the scattering properties of the current voxel.

The difference between $\lambda_0$ for water and materials with mass densities of human tissues (less than 3 gcm$^{-3}$) is smaller than 10%. Hence, the effect of the second approximation on multiple scattering distribution 3.28 is only marginal [50].

The third approximation has the largest effect since it causes a slight overestimation of the lateral deflection angle when the electron is moving from a voxel with high density to a voxel with low density and vice versa. However, the overestimation happens only in *boundaries* of different materials. The multiple scattering in the passed tissues is properly modelled.

## 4.5 DOSE CALCULATION

The absorbed dose, $D = \mathrm{d}E/\mathrm{d}m$, is the expectation value of the energy imparted to matter per unit mass [9]. The absorbed dose from the electron beam can be calculated from the particle fluence as [9,89]

$$D(\mathbf{x}) = \int\int \Phi(\mathbf{x}, \Omega, E) L_{\text{coll}}(E, T_c) \mathrm{d}\Omega \mathrm{d}E. \tag{4.9}$$

In the VMC++ simulation, the absorbed dose in a voxel with a density $\rho$ and volume $\Delta V$ is determined by the path lengths $\Delta \bar{s}_j$ in the voxel and the bremsstrahlung dose profile $D_\gamma(\mathbf{x})$:

$$D(\mathbf{x}) = \sum_j \frac{\Delta \bar{s}_j L_{\text{coll}}(E, T_c)}{\rho \Delta V} + D_\gamma(\mathbf{x}). \tag{4.10}$$

Due to random sampling, there is statistical noise that depends on the number of simulated particles. The statistical uncertainty is usually estimated by dividing the calculation into $n$ batches, say $n = 10$. The uncertainty of the dose in a voxel can be expressed by the standard error of the mean:

$$\bar{\sigma}_D = \sqrt{\frac{\sum_{i=1}^{n} (D_i - \bar{D})^2}{n(n-1)}}. \tag{4.11}$$

# 5 The eMLC prototype and beam model

## 5.1 CONSTRUCTION OF THE PROTOTYPE

The electron multi-leaf collimator prototype (figure 5.1) consists of steel leaves mounted in an aluminium frame. The leaves are 2.0 cm thick and 5.0 mm wide. The prototype was attached below a standard 20×20 cm$^2$ electron applicator type III of a Varian 2100 C/D linac without any modifications for the electron applicator. The source-to-upstream leaf surface distance was 97.2 cm.

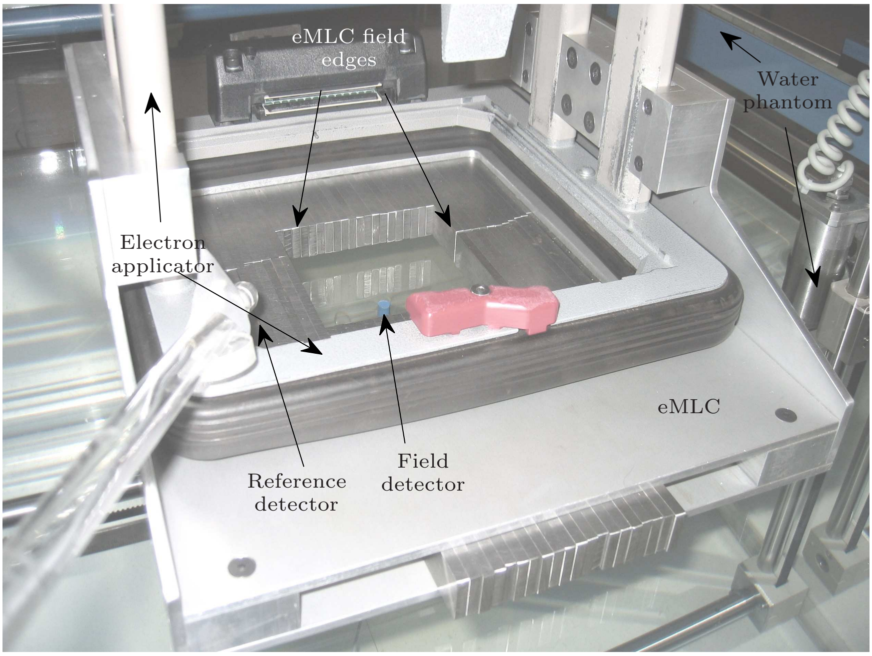

*Figure 5.1: The eMLC prototype attached below the electron applicator of the linac. Leaves of the eMLC can be seen in the aluminium frame below the applicator. Also shown in the figure is the measurement set-up with detectors in a water phantom.*

## 5.2 THE MC BEAM MODEL

The exit phase space plane is defined below the treatment head of the linear accelerator. Therefore, any components that might have an effect on the electron fluence, such as collimators, must be considered in the beam modelling.

The beam model divides the electron fluence emitted from the treatment head into a direct electron fluence component $\Phi_D$ (no collimator interactions, only scattering in air) and an indirect electron fluence component $\Phi_I$ (at least one collimator interaction). In addition, a photon fluence component $\Psi_B$ is applied to account for bremsstrahlung photons:

$$\Phi_{\tilde{S}} = \Phi_D + \Phi_I + \Psi_B. \tag{5.1}$$

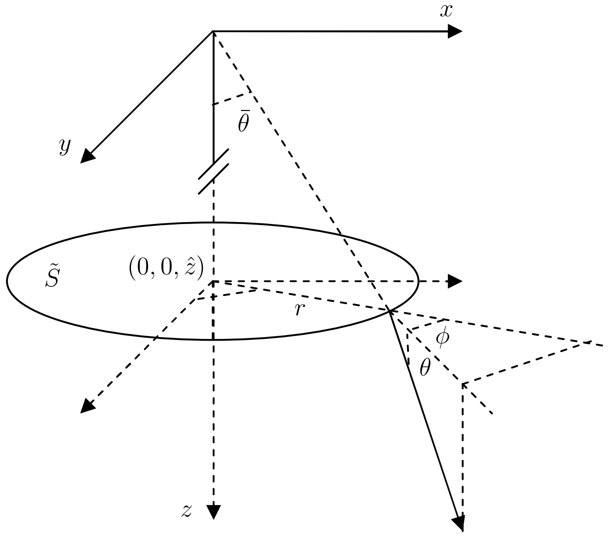

*Figure 5.2: Geometry of the exit phase space plane $\tilde{S}$ located at the distance $\tilde{z}$ from the source at* $(0, 0, 0)$.

### 5.2.1 Modelling of the electron source

The beam model uses multiple sub-sources of electrons with amplitudes coupled to a common source of direct electrons located below the secondary scattering foil [112]. Briefly, electrons with energy $E$ and an energy spectrum $\varphi(E)$ are emitted from the source through the source phase space plane $S(r, \bar{\phi}) = (r\cos\bar{\phi}, r\sin\bar{\phi}, x_{\mathrm{eff}})$, $r \in \mathbb{R}$, $\bar{\phi} \in [0, 2\pi]$. The fluence distribution is symmetrical with respect to $z$-axis (the azimuthal angle $\phi \in [0, 2\pi]$) and the polar angles of electrons $\theta$ are sampled from a Gaussian distribution. Let $\Phi_S(E, \Omega, r)$, $r \in [0, r_{\mathrm{max}}]$ be the phase space density of electrons, also known as fluence differential in energy and angle, in the plane $S$. The electron source is described by the fluence

$$\begin{aligned} &\Phi_S(E,\Omega,r) = \varphi(E)\exp\left(\frac{r^2}{\sigma_r^2} + \sqrt{2}\frac{\phi^2+(\theta-\bar{\theta})^2}{\sigma_{\bar{\theta}}^2(r)}\right), \; r \le r_{\mathrm{max}} \\ &\Phi_S(E,\Omega,r) = 0, \qquad\qquad\qquad\qquad\qquad\qquad r > r_{\mathrm{max}}, \end{aligned} \tag{5.2}$$

where $r$ is the radial distance of the fluence distribution extending to $r_{\mathrm{max}}$ and $\sigma_r \in \mathbb{R}$. The mean angle $\bar{\theta}$ is determined by the effective source position $x_{\mathrm{eff}}$ [112]. The effect of scattering foils, monitor chamber and air on the lateral spread of the fluence distribution is included in $\sigma_{\bar{\theta}}^2(r) = a - br$, $\{a, b\} \subset \mathbb{R}$. Hence, for a fixed energy spectrum, the radial modulation of the phase space density of electrons travelling in the direction $\Omega(\phi, \theta)$ through the source phase space plane $S$ is determined by $\Phi_S := \Phi_{S,\varphi,\Omega}(\sigma_r, a, b, x_{\mathrm{eff}}, r_{\mathrm{max}})$ during the beam characterization process.

### 5.2.2 Exit phase space parameterization

Direct electrons have no interactions with the applicator or eMLC. Electrons hitting the eMLC leaves or applicator elements are scored and terminated. The direct electron fluence differential in energy, angle and position $\Phi_D = \Phi_D(E, \Omega, x, y)$, $\Omega = (\phi, \theta)$ is defined by a lateral fluence distribution and a Gaussian distributed directional spread with a standard deviation $\sigma_\theta$ around an average direction $\bar{\theta}$ given by

$$\bar{\theta}(r) = \tan^{-1}\left(\frac{r}{z_{eff}(r)}\right), \tag{5.3}$$

where $r = (x^2 + y^2)^{1/2}$ is the distance from the beam axis (figure 5.2) and $z_{eff}(r)$ is the distance to a virtual source point located

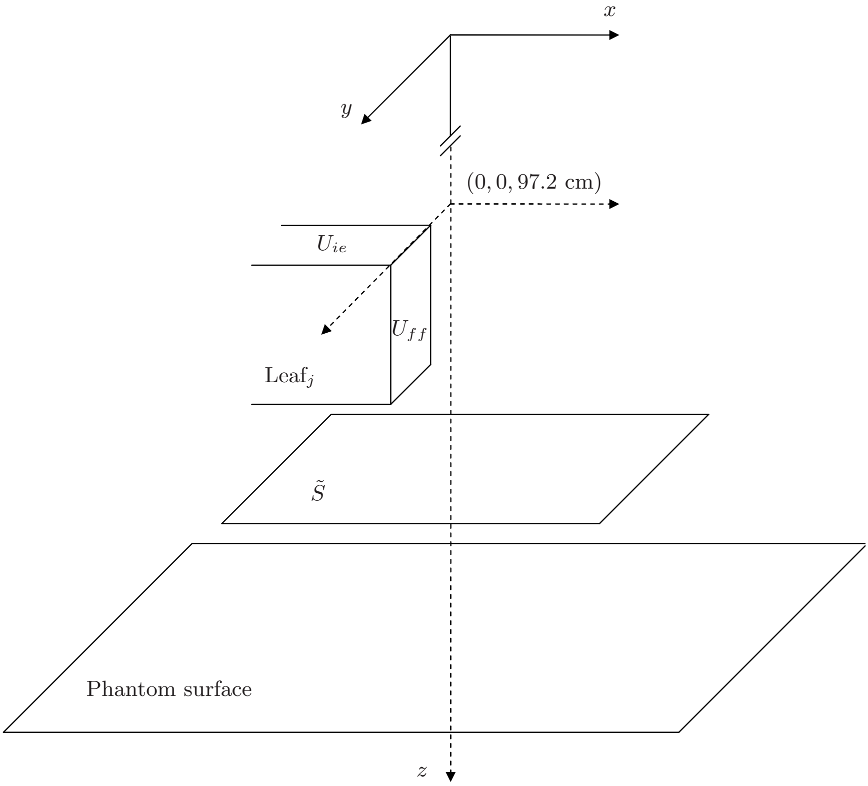

*Figure 5.3: Schematic presentatation of the eMLC leaf geometry for the leaf j with the inner edge surface* $U_j^{ie}$ *and front face surface* $U_j^{ff}$.

on the beam axis upstream from the exit phase space plane. The Gaussian distributed spread $\sigma_\theta = \sigma_\theta(r)$ is a function of the distance from the beam axis. The functions $z_{eff}(r)$ and $\sigma_\theta(r)$ are determined by scoring the exit directions on a set of beam axis centered, annular rings [112].

### Electron out-scatter modelling

A direct electron hitting an upstream collimating aperture has a certain probability of being out-scattered back into the field and thereby constituting a source of indirect electrons. For the current eMLC, one should consider this kind of out-scatter from the eMLC leaves and from the two upstream applicator scraper layers. Since the eMLC device is effectively shadowing the lowermost scraper below which the eMLC is mounted, the out-scatter from this layer need not to be considered.

One can identify two distinct cases leading to out-scatter, namely grazing incidence on the front face $(ff)$ and near perpendicular incidence on the inner edge $(ie)$ surface of the scattering object [1,111]. Accordingly, the indirect fluence differential in energy and angle $\Phi_I$ at a point $\mathbf{p} = (x, y, \tilde{z})$ in the exit phase space plane $\tilde{S}$ is separated into fluences $\Phi_I^{ie}$ and $\Phi_I^{ff}$ such that

$$\Phi_I(\mathbf{p}) = \sum_{l=2}^{3}\sum_{k=1}^{4}\left(\Phi_{I,l,k}^{ie}(\mathbf{p}) + \Phi_{I,l,k}^{ff}(\mathbf{p})\right) + \sum_{j=1}^{N}\left(\Phi_{I,j}^{ie}(\mathbf{p}) + \Phi_{I,j}^{ff}(\mathbf{p})\right), \tag{5.4}$$

where the subscripts $l$ and $k$ refer to the two upstream scraper layers and the four sides of each aperture, respectively. The summation in the right term runs over all eMLC leaf sides $j = 1, \ldots, N$ facing the open part of the field. The indirect fluence $\Phi_I$ is reconstructed by sampling from pre-calculated edge scatter kernels following the principles presented by Ahnesjö [1] and Traneus et al. [111] using separate scatter kernels $\kappa^{ie}$ and $\kappa^{ff}$ for the inner edge and front face surfaces, respectively. The scatter kernels are calculated using the EGSnrc code [57].

The characteristics of the leaf out-scatter depend on the incident electrons energy, leaf thickness and the electron incidence angle and position. For the inner edge case, the electrons hit the surface at an approximately perpendicular angle. Since the inner edge out-scatter is only weakly dependent on the incidence angle, one can assume that the electrons hit the inner edge surface at a perpendicular angle and therefore a single inner edge kernel is sufficient. For the front-face case, it is possible to assume that the front-face surface is infinite, thus neglecting transmission through the downstream edge and effects of nearby corners. As the front-face out-scatter probability is strongly dependent on the incidence angle between the direction of the electron and the front-face surface one can apply a set of front-face kernels generated for a discrete set

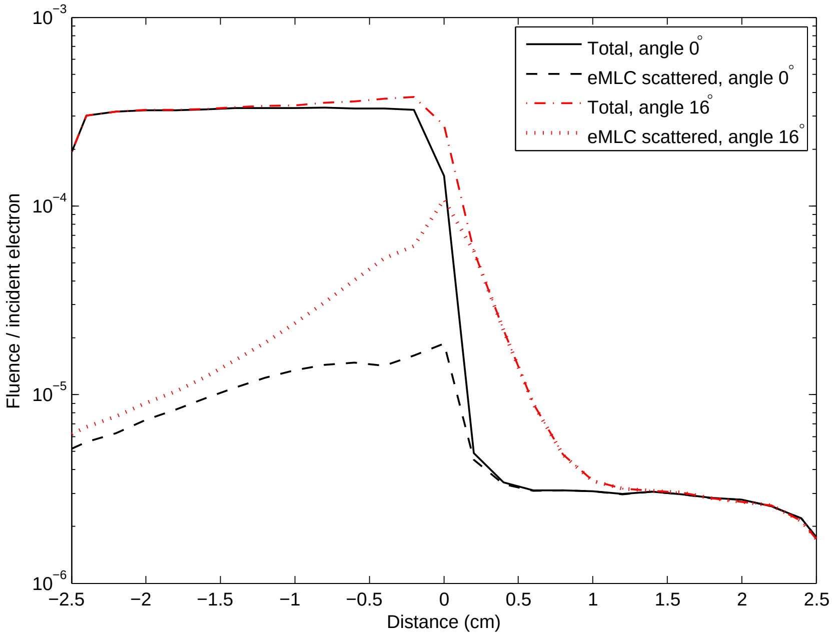

*Figure 5.4: BEAMnrc calculated total and eMLC scattered electron fluence in air for different beam incidence angles. Field size is 5×10 cm$^2$ and the field edge is at zero position.*

of incidence angles ranging from 1° to 16°. This angle range was selected since it includes the scatter from the lowermost applicator scraper. Figure 5.4 shows electron fluence below the eMLC for different beam incidence angles.

Let $U_j^{ie}$ and $U_j^{ff} \subset \mathbb{R}^2$ be the front face, inner edge and leaf side surfaces for the leaf $j$, $j = 1, \ldots, N$ (figure 5.3). For a full description of the scatter kernels, one needs to determine, how much the fluence on element areas $\Delta U_j^{ie}$ and $\Delta U_j^{ff}$ at points $\mathbf{u}_j^{ie} = (u_{ie,1,j}, u_{ie,2,j})$ and $\mathbf{u}_j^{ff} = (u_{ff,1,j}, u_{ff,2,j})$ contribute on the exit phase space density at a point $\mathbf{x} = (x_1, x_2, \tilde{x})$ in the exit phase space plane $\tilde{S}$. The phase space densities in points $\mathbf{u}_j^{ie}$ and $\mathbf{u}_j^{ff}$ at the front face and inner edge are $\Phi(\mathbf{u}_j^{ie})$ and $\Phi(\mathbf{u}_j^{ff})$, respectively. Once the scatter kernels are known, the phase space density for leaf scattered electrons from

$N$ leaves can be calculated from the usual convolution such that

$$\Phi_{I,4}(\mathbf{x}) = \sum_{j=1}^{N} \left[ \int_{U_j^{ie}} \kappa^{ie}(\mathbf{x}, \mathbf{u}_j^{ie}) \Phi(\mathbf{u}_j^{ie}) \mathrm{d}\mathbf{u}_j^{ie} + \int_{U_j^{ff}} \kappa^{ff}(\mathbf{x}, \mathbf{u}_j^{ff}) \Phi(\mathbf{u}_j^{ff}) \mathrm{d}\mathbf{u}_j^{ff} \right]. \quad (5.5)$$

## 5.3 VERIFICATION OF THE BEAM MODEL

The agreement between calculated and measured dose distributions was evaluated according to Low et al. [74] by using the gamma index. It is defined for a fixed allowable deviation in distance, $\Delta d_{\mathrm{M}}$, and dose $\Delta D_{\mathrm{M}}$ for the calculated and measured doses $D_{\mathrm{c}}(\mathbf{x}_{\mathrm{c}})$ and $D_{\mathrm{m}}(\mathbf{x}_{\mathrm{m}})$ in points $\mathbf{x}_{\mathrm{c}}$ and $\mathbf{x}_{\mathrm{m}} \in \mathbb{R}^2$ as

$$\gamma(\mathbf{x}_{\mathrm{m}}) = \min\{\Gamma(\mathbf{x}_{\mathrm{m}}, \mathbf{x}_{\mathrm{c}})\}, \ \forall \ \mathbf{x}_{\mathrm{c}}, \quad (5.6)$$

where

$$\Gamma(\mathbf{x}_{\mathrm{m}}, \mathbf{x}_{\mathrm{c}}) = \left( \frac{\|\mathbf{x}_{\mathrm{c}} - \mathbf{x}_{\mathrm{m}}\|^2}{\Delta d_{\mathrm{M}}^2} + \frac{(D_{\mathrm{c}}(\mathbf{x}_{\mathrm{c}}) - D_{\mathrm{m}}(\mathbf{x}_{\mathrm{m}}))^2}{\Delta D_{\mathrm{M}}^2} \right)^{1/2}. \quad (5.7)$$

The units for $\Delta d$ and $\Delta D$ are millimeter and percent. Hence, for values $\gamma \leq 1$, the calculated dose is within certain acceptance criteria, say 2% and 2 mm. Depth dose curves were measured with the Scanditronix PPC-40 parallel plate ionization chamber and profiles were acquired with the PTW-31 006 pinpoint chamber in water.

## 5.4 COMPARISON OF CONVENTIONAL INSERTS AND THE eMLC

For the electron beam shaping 1.5 cm thick individually made Cerrobend® inserts mounted in a standard 20×20 cm$^2$ electron applicator of a Varian 2100 C/D linac were used. The insert and eMLC fields were compared in the situation of chest wall irradiation. With a standard applicator the distance from focus to the lower surface of the insert was 95 cm i.e. the collimator-to-surface distance (CSD) was 5.8 cm at the applied treatment distance (SSD = 100.8 cm). The adjacent electron fields shared the same virtual source position such that the abutting field edges coincided and the isocenter was the same for both electron and photon fields (figure 5.5).

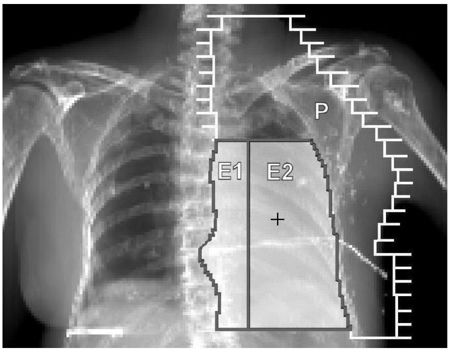

*Figure 5.5: Beams eye-view of the chest wall irradiation for breast cancer with adjacent electron beams E1 and E2 together with a matched photon beam (P).*

## 5.5 SIMULATIONS AND MEASUREMENTS OF DIFFERENT LEAF SHAPES AND MATERIALS

Depth dose curves and profiles were measured with the Scanditronix SFD diode detector in water for narrow fields with sizes from $0.3\times10$ cm$^2$ to $1.5\times10$ cm$^2$. The voxel sizes in the VMC++ simulations were $1\times1\times1$ mm$^3$ and $1\times2\times2$ mm$^3$ for the 6 and 9 MeV energy.

The properties of the straight, round and 15° face angle leaf ends for 6, 12 and 20 MeV electron beam were investigated using the BEAMnrc code revision 1.78 [103]. The eMLC with leaf materials made of steel, brass and tungsten were included in the model. The energy of the source electrons exiting from the vacuum was adjusted such that the calculated and measured depth dose for the $5\times5$ cm$^2$ field agreed to within 1%. The cut-off energies for electrons (ECUT) and photons (PCUT) were 0.521 and 0.01 MeV, respectively. These same values were also applied for the threshold energies $T_c$ and $k_c$. In the simulations, the EXACT boundary crossing and the PRESTA-II electron-step algorithm were used.

## 5.6 RESULTS

### 5.6.1 Verification of the beam model

The depth dose curves for different field sizes and energies 6, 12 and 20 MeV at SSD 100 cm are presented in figure 5.6 for the eMLC prototype with steel leaves. The profiles close to the depth of dose maximum and a superficial profile at 0.5 cm depth are shown in figure 5.7 where only half profiles are shown because of the symmetry. The calculated depth dose was slightly underestimated near to the surface of the phantom (I). This effect was pronounced with high energies and small field sizes such that for the 20 MeV $5\times5$ cm$^2$ field, the calculated dose was underestimated by up to 8% while for other energies and field sizes, the maximum deviations were less than 5% and there was a good agreement between the calculated and the measured dose. At the beam axis, the indirect dose component increased with the decreasing field size as the front face out-scatter dominated and was more forward peaked compared to the inner edge out-scatter (I).

The calculated profiles near the dose maximum depth were slightly underestimated with small field sizes and high energies (I). However, the agreement between calculated and measured profiles in the penumbral region was excellent except for the $20\times20$ cm$^2$ field. The calculated indirect electron component increased near to the field edges (I).

In total, 88% and 95% of the voxels were within 2%/2 mm and 3%/3 mm acceptance criteria. In 89% of the voxels, the dose difference was within ±3%.

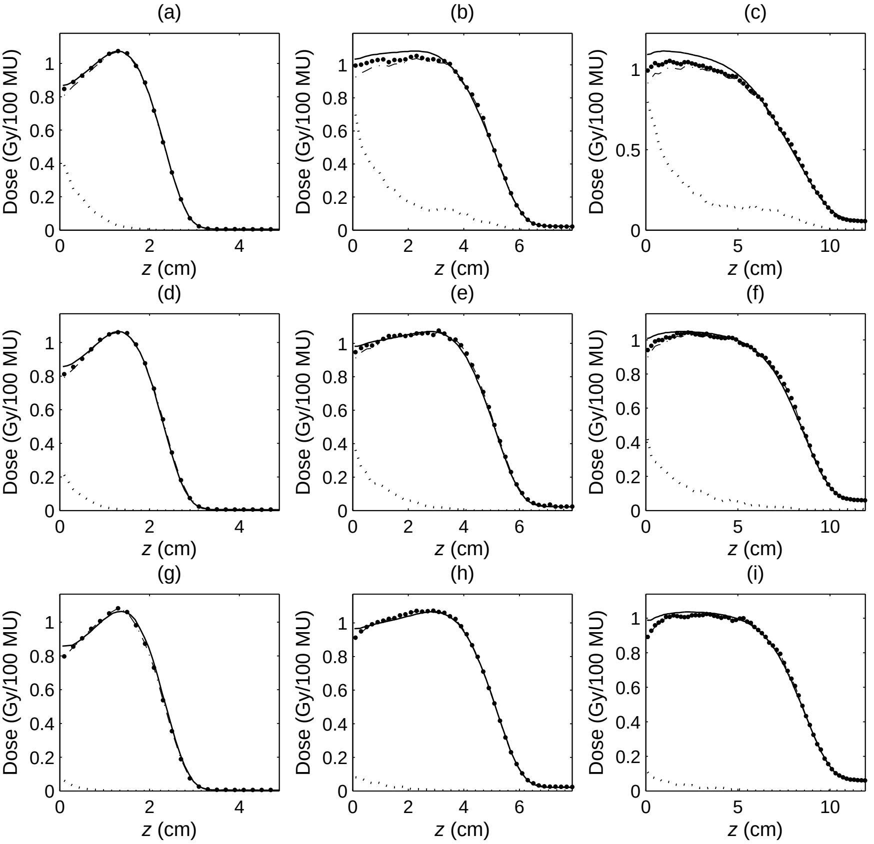

*Figure 5.6: Calculated (·) and measured (–) depth dose curves for (a)-(c) 5×5 cm$^2$ field; (d)-(f) 10×10 cm$^2$ field and (g)-(i) 20×20 cm$^2$ field at SSD 100 cm for energies (a), (d), (g) 6 MeV; (b), (e), (h) 12 MeV; (c), (f), (i) 20 MeV. The doses from direct electrons (dash-dotted line) and indirect collimator scattered electrons (light-dotted line) are plotted separately. The dose from the indirect electrons is plotted multiplied by ten.*

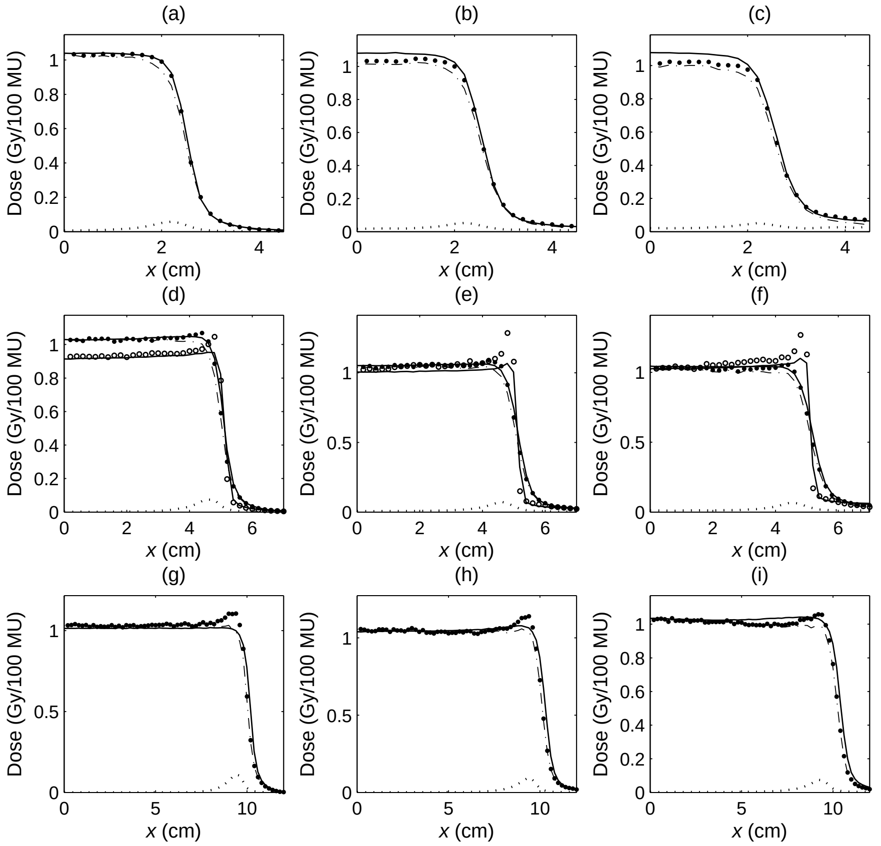

*Figure 5.7: Calculated (·) and measured (–) profiles for (a)-(c) 5×5 cm$^2$ field; (d)-(f) 10×10 cm$^2$ field and (g)-(i) 20×20 cm$^2$ field at SSD 100 cm for energies (a), (d), (g) 6 MeV at 1.0 cm depth; (b), (e), (h) 12 MeV at 2.0 cm depth and (c), (f), (i) 20 MeV at 3.0 cm depth. A superficial profile at 0.5 cm depth is plotted for the 10×10 cm$^2$ field (open circles). The doses from direct electrons (dash-dotted line) and indirect collimator scattered electrons (light-dotted line) are plotted separately. The profiles are for the eMLC prototype with steel leaves.*

### 5.6.2 Comparison of conventional inserts and the eMLC

When two abutting electron–electron or electron–photon fields are matched, there are dose maximum and minimum areas in the field junction (II). Figures 5.8 and 5.9 illustrate unpublished profiles for matched electron–electron and electron–photon fields with the same isocenter. In figure 5.8, there are dose maxima 110% and 105% and minimima 70% and 80% for insert and the eMLC prototype with 6 and 12 MeV energy, respectively. The dose uniformity can be improved by overlapping the abutting electron field edges or leaving a gap between them (figure 5.8).

In the case of matched electron–photon fields, the uniformity of the dose is markedly better with the eMLC than for the insert close to the 6 MeV electron beam dose maximum depth (1 cm). However, at 2 cm depth, the uniformity is similar between the collimators (figure 5.9).

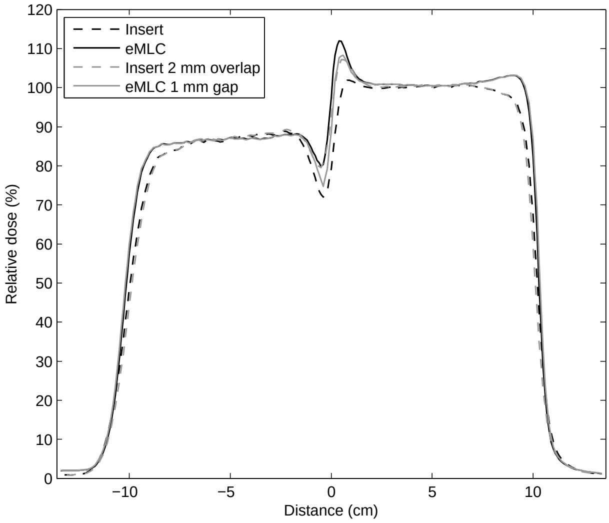

*Figure 5.8: Matched 6 and 12 MeV electron fields normalized to 100% at dose maximum depth. Field sizes are 10×20 cm$^2$ and the profiles are measured at 2 cm depth in water with SSD 100 cm.*

In the dose distribution for the eMLC, the dose was slightly pronounced near the edges of the adjacent electron fields compared

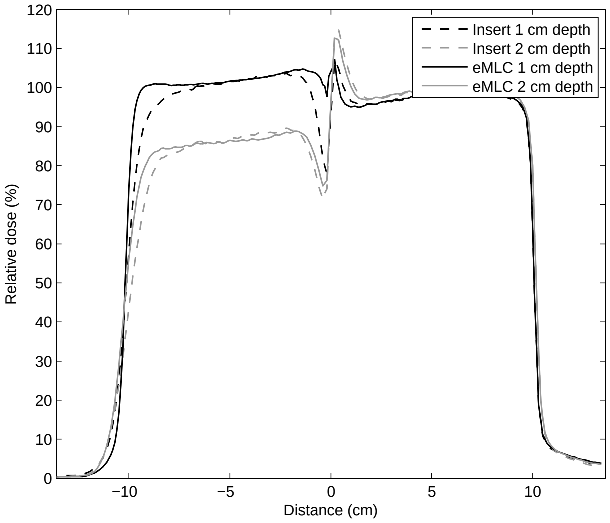

*Figure 5.9: Matched 6 MeV electron and 6 MV photon fields normalized to 100% at dose maximum depth. Field sizes are 10×20 cm$^2$ and the profiles are measured at SSD 100 cm in a water phantom.*

to the insert plan (figure 5.10). In addition, the mean and maximum PTV doses were slightly higher for the eMLC plans (II). The mean calculation time per electron beam for the insert plans was 10.7 minutes compared to 14.8 minutes for the eMLC plans with 1% statistical uncertainty of the dose. At a 2% uncertainty level, the mean calculation times were decreased by more than half (II).

### 5.6.3 Build-up dose of narrow beams

Figure 5.11 illustrates the calculated and measured central axis depth dose curves for 6 and 9 MeV energies with various field widths at SSD 105 cm. With the 1.5 cm wide beams, the build-up region was clearly detectable but for the 1.0 cm beams the dose at the build-up region was within 90% of the depth dose maximum. The build-up region almost disappeared with the 0.5 and 0.3 cm beams but at the expense of a marked decrease in the therapeutic range. The calculated depth doses agreed to within 2 mm of the measured dose in 93.2% of the voxels, whereas 85.1% of the voxels were within 3%

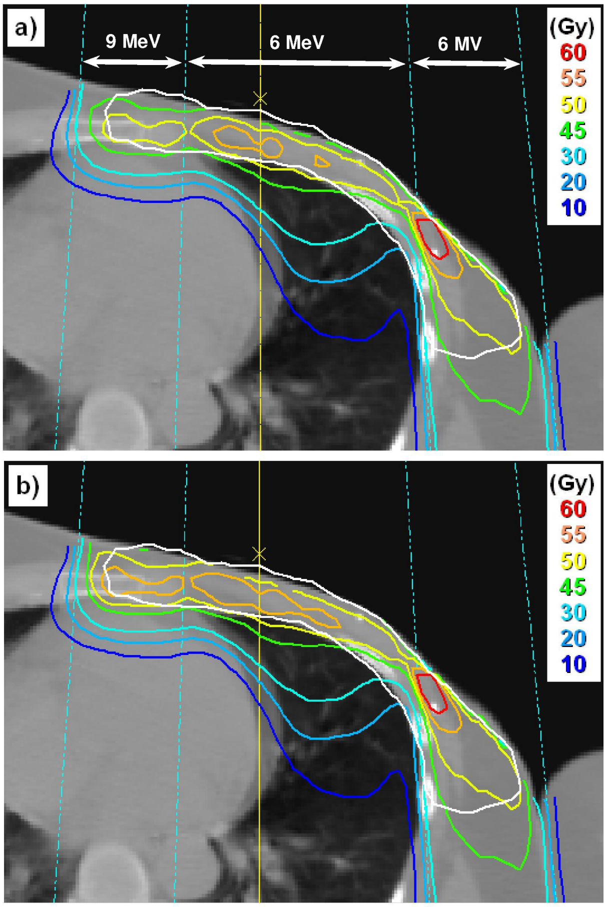

*Figure 5.10: Calculated dose distributions in the chest wall for one of the patients with 6 and 9MeV electrons and 6 MV photons, (a) insert plan and (b) eMLC plan with steel collimator leaves. The PTV is marked with a white line. The VMC++ algorithm was applied to calculate electron fields and a pencil beam algorithm was used for the photon field.*

dose difference.

For a composite segmental field formed from adjacent beam segments, the surface dose at 0.5 mm depth was increased as compared to a size-equivalent open, single field (III). With the segmental field technique, the resulting decrease in the therapeutic range was less than 2 mm compared to a 6 MeV open field. The increase in the surface dose depended on the individual segment width and SSD. The surface dose at the level of 90% of the depth dose maximum was found for the segmental fields with 0.5 and 1.0 cm wide segments at SSD 102 cm (III). With SSD 105 cm, the surface dose was similar to an open field of the same size with 6 MeV energy.

### 5.6.4 Leaf shape and material

The leaf material had only a slight effect on the fluence for straight and round leaves for a 6 MeV electron beam (IV). With 15° face angle leaves made of tungsten, the total fluences at 1 cm outside field edge were 38%, 54% and 59% lower compared with steel and brass for 6, 12 and 20 MeV (IV). Hence, the fluence distributions for tungsten leaves are more focused compared to steel and brass. This was more clearly seen with the higher beam energy and a larger face angle.

With a 6 MeV energy, the 15° face angle leaves led to increased dose per simulated particle in the build-up region and at a dose maximum compared to other leaf shapes (IV). The depth dose was almost identical with straight and round leaves for both SSD 102 and 105 cm. With the 15° face angle leaves, the build-up dose varied between 91-100% and with other leaf shapes between 90-100% (SSD 102 cm) and 89-100% (SSD 105 cm). There was no difference in the dose from bremsstrahlung photons, i.e in the tails of the depth dose curves between fields with different leaf geometries (IV). With straight, round and 15° face angle leaves, the doses at 1 cm outside field edge were 4.6, 5.0 and 6.6% of the central axis at SSD 102 cm, respectively. Hence, the scatter arising from the round and 15° face angle leaves can be observed in profiles. Despite a 1 mm deviation

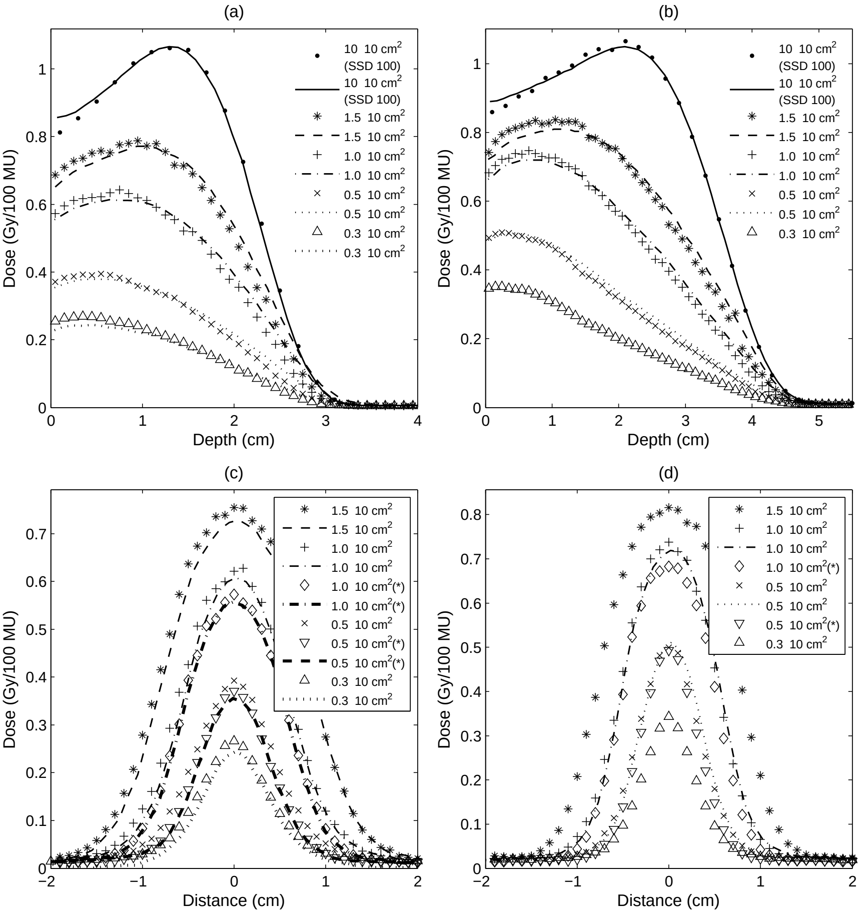

*Figure 5.11: Effect of field width on calculated (symbols) and measured (lines) depth doses (a), (b) and profiles (c), (d) with beam energies (a), (c) 6 MeV and (b), (d) 9 MeV at SSD 105 cm. The depth dose curves and profiles are for the eMLC prototype with steel leaves. The dose calculations were done using the VMC++ algorithm.*

in the build-down region, the agreement between calculated and measured depth doses and profiles was good for a narrow field with straight eMLC leaf ends (IV).

For 12 MeV energy with the 15° face angle leaves, the build-up dose varied between 95-100% and with other leaf shapes between 94-100% at SSD 102 and 105 cm (IV). With straight and round leaves, the dose at 1 cm outside field edge was 8.3% of the central axis compared with 11.3% for 15° leaf face angle at SSD 102 cm. Hence, the scatter from the round and 15° face angle leaves can also be seen in 12 MeV profiles (IV).

With a 20 MeV beam energy, the build-up dose varied between 94-100% for all leaf shapes at SSD 102 and 105 cm (IV). With straight, round and 15° face angle leaves, the doses at 1 cm outside field edge were 6.4, 5.9 and 9.6% of the central axis at SSD 102 cm, respectively. Therefore, the scatter and leaf transmitted electrons arising from the 15° face angle leaves can be more clearly seen in the 20 MeV profiles (IV).

The summed depth doses from five narrow abutting 6 MeV energy $1 \times 10$ cm$^2$ fields were normalized to the depth dose maximum. With the 15° face angle leaves, the build-up dose at 5 mm depth is 96% of the depth dose maximum at SSD 102 cm (IV) compared with 86% for straight and round leaves. Simultaneously, the therapeutic range is reduced by less than 1 mm. At SSD 105 cm, the 6 MeV build-up dose at 5 mm depth was still higher by four percentage units for the 15° face angle compared with the other leaf ends (IV).

# 6 Discussion

An eMLC prototype was developed as an alternative for use with the present collimation of electron beams with block inserts. Monte Carlo dose calculation was applied to the eMLC beam for accurate modelling of the dose. Dosimetry of the eMLC and the accuracy of the beam model were studied by comparing the calculated and measured dose in water.

For a beam model aimed at clinical use, a compromise has to be made between the accuracy and complexity of the model. The kernel model with relevant scatter kernels was chosen to calculate the leaf scattered indirect electron component to enable faster computation. The calculations were evaluated against measurements with good accuracy since 88% of the voxels were within 2%/2 mm. This was comparable to previously reported calculations for electron inserts with various beam energies, field sizes and SSD [18]. With the VMC++ algorithm, there are some approximations that make the simulation rapid to perform. However, with typical radiotherapy energies ($< 20$ MeV) and tissue densities ($< 3$ gcm$^{-3}$), the simplifications lead to a minor loss of accuracy (1%) for electron transport [28, 50, 55]. The resulting effect on the accuracy of calculated dose is only minimal, only 2% [18, 19, 28, 50, 55]. In particular, the modelling of lateral and longitudinal energy loss straggling with the VMC++ is very good, with only a 2% variation of the calculated electron position as a function of energy loss per step [48].

The prototype add-on eMLC was implemented below a standard electron applicator without modifications for the applicator. Ma et al. [81] and Ravindran et al. [100] used a slightly different solution where the eMLC was inside the applicator and closer to the electron source. One drawback from the present short (8 mm) collimator-to-surface distance was a pronounced dose near the field edges at SSD 100 cm as shown in the original publication I. This "horn" effect has been previously reported by Lee et al. [70] and

Ravindran et al. [100] who found that the short CSD resulted in smaller penumbras. The leaf transmission with high energies (6.3% with 20 MeV) can be reduced using an appropriate leaf material and leaf thickness.

At SSD 110 cm, the agreement between calculated and measured depth doses was practically the same as with SSD 100 cm for different beam energies. In spite of a slight overestimation of calculated dose near to the edge of the field, the agreement was good also with tested irregular fields (I).

The fluence distribution of the leaf-scattered electrons depends on beam energy, leaf material, thickness and field shape. For electrons incident to the leaf front face, the out-scatter probability depends strongly on the incidence angle distribution. Overall, there was a good agreement between calculated and measured dose for most clinically relevant energies between 6–12 MeV, field sizes and SSD. For small square fields with 20 MeV energy, the calculated depth doses were underestimated. The deviations observed in the penumbral region of the 20×20 $\text{cm}^2$ field may be due to scattered electrons from the upstream applicator structures. In the beam model, the electrons are emitted from the downstream surface of the leaves. By emitting the electrons by distributing them uniformly over the full leaf thickness, the penumbral region could be better modelled. Additionally, the fact that the bremsstrahlung from the eMLC leaves was not explicitly included in the VMC++ dose calculations may explain some of the deviations in particular with 16-20 MeV energies.

Electron beam patient dose calculations for an add-on multi-leaf collimator prototype were compared with the conventional electron inserts in chest wall irradiation of left-sided breast cancer (II). Between matched, abutting fields, the dose profiles are not uniform (figures 5.8 and 5.9). There are different methods for smoothing the dose distribution in the junction area, for example overlapping the fields or leaving a gap between them [110].

The mean PTV and OAR doses were slightly higher for the eMLC generated plans (II). The largest differences accounting for approximately 4% of the prescribed dose were found in the mean dose and in the high dose region of the PTV (D5%, D10%). For both the left lung, and heart the differences were small (0.5% or even less). The slightly higher dose for the eMLC compared to the insert plans may be due to a different shape of the eMLC field (saw-toothed edges), a different source-to-collimator distance or different thicknesses and materials of the collimators. However, the particle fluence with low energy eMLC beams are smooth already at the surface [81] and the saw-toothed field shape is not seen in isodoses at the dose maximum depth [70].

Using the same CSD 5.8 cm for both collimators leaves enough space for patient positioning. A longer CSD (e.g. 10 cm) would likely have lead to differences in the penumbra and dose inside the field edge even smaller.

The possibility to increase the dose in the build-up area of the electron depth dose curve was studied by using adjacent narrow beam segments with a width from 0.3 cm to 1.5 cm (III). The accuracy of the beam model for the narrow beams was good since the VMC++ dose calculations and measurements agreed within 2 mm in 93.7% of the voxels. This was comparable to previously reported calculations for electron inserts [18, 19, 87, 107, 111]. The build-up dose was enhanced due to the absorption of direct electrons by the eMLC, edge scatter and collimator transmission. Beam segments with a width less than 1.0 cm at SSD 102 cm have a surface dose more than 90% of the depth dose maximum. At a longer SSD 105 cm, the surface dose is increased only modestly compared with the open field of the same size (III). For the segmental field with 1.0 cm wide segments at SSD 102 cm, the surface dose and target coverage was comparable to a 0.5 cm thick bolus. With the 1 cm wide segment the therapeutic range was not markedly reduced compared to an open field (III). The reduction was clearly evident with narrower fields.

The dose from bremsstrahlung photons with 6 MeV electrons was 4% for the $9\times10$ cm$^2$ field (1.0 cm wide segments). The photon dose may limit the use of the segmental field technique in some cases since the amount of treatment head generated bremsstrahlung increases with the number of segments due to leaf transmission. However, the photon dose could be reduced by using thicker leaves made of high-Z material.

Flatness for the segmental field profiles was slightly worse than with a size-equivalent open field (III). Summing of various small fields and energies, with the weights determined by inverse optimization similar to the proposal of Al-Yahya et al. [2, 3] might, result in improved profiles.

The effects of the leaf shape and material were studied by a BEAMnrc treatment head model and there was found to be an excellent agreement between calculated and measured dose (IV). A field size of $1\times10$ cm$^2$ was selected to study the effect of leaf shape since the differences should be most evident with a narrow field. With the 15° face angle leaves pointing towards the beam axis, the build-up dose was higher as compared to straight and round leaf shape for narrow eMLC fields.

There were only minor differences in fluence and angle distributions between different leaf materials for 6 MeV beam energy. With tungsten, the total fluences at 1 cm outside of the $1\times10$ cm$^2$ field were 54% and 59% lower compared with steel and brass for 12 and 20 MeV. With high energies, the fluence and angle spectra were more peaked for tungsten than other materials (IV). Similar to the report of Ma et al. [81], leaves made of steel resulted in slightly wider fluence distribution than tungsten. Additionally, for the 15° face angle the mean energy for brass was identical to steel with 6 MeV.

In the energy spectra for different leaf shapes, the 15° face angle leaves had a slightly wider spectrum compared with straight and round leaves. With the 15° face angle leaves, there were more electrons scattered at wide angles below the eMLC compared to straight and round leaves (IV). In addition, there were more low energy electrons in the energy spectrum for the 15° face angle leaves. For five abutting 6 MeV fields, the 15° face angle leaves resulted in a 96% build-up dose at 5 mm depth, which was ten percentage units higher than with round or straight leaves. However, the effect was reduced to 89% build-up dose at 5 mm depth with 15° face angle leaves compared with 85% for other leaf shapes for SSD 105 cm (IV). This was due to scattering of electrons in the air gap between the eMLC and the phantom surface. Because of the low energy of these electrons, they had only a slight effect (less than 1 mm decrease) on the therapeutic range.

The effect of eMLC leaf shape on build-up dose at 5 mm depth was between 3-4% units with 12 MeV at SSD 105 cm. At SSD 102 cm and for 20 MeV beam energy, the effect was only marginal. Since bremsstrahlung photons from the treatment head are known to be produced mainly in the scattering foils of the linac in electron beams [92, 109], the photon tail in depth dose curves was of the same order for all leaf shapes.

In summary, the eMLC is potentially feasible for electron beam collimation. Although in a typical treatment, there are no major differences compared to insert-based collimation, the profiles are slightly pronounced near to the field edges at SSD 100 cm. This effect should be considered when matching the eMLC beams. In the segmental field technique, the dose in the build-up area of the depth dose curve was increased. The cost was a minor reduction of the therapeutic range and summing the dose from leaf transmitted photons. Since the bremsstrahlung dose was only a fraction of the build-up maximum dose due to a low beam energy, segmental fields might be considered as a choice for using a bolus on the skin.

# 7 Conclusions

Electron beam collimation with an add-on type eMLC is a feasible technique. In a clinical case of the chest wall irradiation, there are no major differences in dose distributions from the eMLC compared to the present collimation with low melting point inserts.

Modelling of the eMLC beam can be performed with a good accuracy by a parametrized Monte Carlo beam model. In addition the calculation time is short enough for clinical use with the VMC++ algorithm. Thus the beam model may be further developed for clinical application. However, some improvements will be needed in modelling the small square fields of high energy (16-20 MeV).

Build-up dose of narrow composite segmental eMLC fields is markedly enhanced compared with the situation in a large field. The advantage of this is that one achieves a higher dose to the target volume near to the skin surface at the cost of dose homogeneity in the abutting fields. The segmental $9\times10$ cm$^2$ field formed from $1\times10$ cm$^2$ segments results in a build-up dose that is comparable to the bolus technique. The segmental fields may be considered as a choice for using a bolus on the skin.

The shape of the eMLC leaf has a marked effect on the build-up dose with narrow fields. A 15° angle leaf end can result in a surface dose which is up to 91% of the dose maximum. A device equipped with motorized leaves would facilitate the clinical use of the eMLC.

# References

[1] A. Ahnesjö. Collimator scatter in photon therapy beams. *Med Phys*, 22(3):267–278, 1995.

[2] K. Al-Yahya, D. Hristov, F. Verhaegen, and J. Seuntjens. Monte Carlo based modulated electron beam treatment planning using a few-leaf electron collimator - feasibility study. *Phys Med Biol*, 50(5):847–857, 2005.

[3] K. Al-Yahya, M. Schwartz, G. Shenouda, F. Verhaegen, C. Freeman, and J. Seuntjens. Energy modulated electron therapy using a few leaf electron collimator in combination with IMRT and 3D-CRT: Monte Carlo-based planning and dosimetric evaluation. *Med Phys*, 32(9):2976–2986, 2005.

[4] K. Al-Yahya, F. Verhaegen, and J. Seuntjens. Design and dosimetry of a few leaf electron collimator for energy modulated electron therapy. *Med Phys*, 34(12):4782–4791, 2007.

[5] H. Alasti and D.M. Galbraith. Depth dose flattening of electron beams using a wire mesh bolus. *Med Phys*, 22(10):1675–1683, 1995.

[6] S.J. Allen, E.E. Klein, M. Michaletz-Lorenz, and J.Y. Jin. Comparison of two treatment techniques for breast irradiation including internal mammary nodes. *Med Dosim*, 29(2):124–7, 2004.

[7] P. Andreo. Monte Carlo techniques in medical radiation physics. *Phys Med Biol*, 36(7):861–920, 1991.

[8] J.O. Archambeau, B. Forell, R. Doria, D.O. Findley, R. Jurisch, and R. Jackson. Use of variable thickness bolus to control electron beam penetration in chest wall irradiation. *Int J Radiat Oncol Biol Phys*, 7(6):835–842, 1981.

[9] F.H. Attix. *Introduction to Radiological Physics and Radiation Dosimetry*. John Wiley & Sons, Inc., New York, 1986.

[10] F.H. Attix and W.C. Roesch, editors. *Radiation dosimetry, Vol. 1, Fundamentals, 2nd ed.* Academic Press, Inc., New York, 1968.

[11] M. Berg and O. Noerrevang. Recombination factors for the cylindrical FC65-G ionization chamber in pulsed photon beams and the plane-parallel roos ionization chamber in pulsed electron beams. *Phys Med Biol*, 49(23):5309–5318, 2004.

[12] M.J. Berger, J.S. Coursey, M.A. Zucker, and J. Chang. *Stopping-Power and Range Tables for Electrons, Protons, and Helium Ions*. The National Institute of Standards and Technology (NIST), 2005 (Online: http://www.nist.gov/physlab/data/star/index.cfm).

[13] M. Blomquist, M.G. Karlsson, B. Zackrisson, and M. Karlsson. Multileaf collimation of electrons - clinical effects on electron energy modulation and mixed beam therapy depending on treatment head design. *Phys Med Biol*, 47(7):1013–1024, 2002.

[14] E. Boman. *Radiotherapy Forward and Inverse Problem Applying Boltzmann Transport Equation*. Doctoral dissertation, Kuopio University Publications C. Natural and Environmental Sciences 204. University of Kuopio, Kuopio, Finland, 2007.

[15] A. Brahme, editor. Accuracy Requirements and Quality Assurance of External Beam Therapy with Photons and Electrons. *Acta Oncol*, 27(Suppl. 1):1–79. 1988.

[16] A. Brahme, I. Lax, and P. Andreo. Electron beam dose planning using discrete gaussian beams. mathematical background. *Acta Radiol Oncol*, 20:147–158, 1981.

[17] M. Cederbaum, A. Ravkin, E. Rosenblatt, and E. Gez. Implementing a tantalum wire mesh to increase the skin dose in low-energy electron irradiation of the chest wall. *Med Dosim*, 26(3):275–279, 2001.

[18] J.E. Cygler, G.M. Daskalov, G.H. Chan, and G.X. Ding. Evaluation of the first commercial Monte Carlo dose calculation engine for electron beam treatment planning. *Med Phys*, 31(1):142–153, 2004.

[19] J.E. Cygler, C. Lochrin, G.M. Daskalov, M. Howard, R. Zohr, B. Esche, L. Eapen, L. Grimard, and J.M. Caudrelier. Clinical use of a commercial Monte Carlo treatment planning system for electron beams. *Phys Med Biol*, 50(5):1029–1034, 2005.

[20] J. Deng, M.C. Lee, and C.-M. Ma. A Monte Carlo investigation of fluence profiles collimated by an electron specific MLC during beam delivery for modulated electron radiation therapy. *Med Phys*, 29(11):2472–2483, 2002.

[21] G.X. Ding, J.E. Cygler, C.W. Yu, N.I. Kalach, and G. Daskalov. A comparison of electron beam dose calculation accuracy between treatment planning systems using either a pencil beam or a Monte Carlo algorithm. *Int J Radiat Oncol Biol Phys*, 63(2):622–633, 2005.

[22] G.X. Ding, J.E. Cygler, G.G. Zhang, and M.K. Yu. Evaluation of a commercial three-dimensional electron beam treatment planning system. *Med Phys*, 26(12):2571–2580, 1999.

[23] N. Dogan, L.B. Leybovich, A. Sethi, and B. Emami. Improvement of dose distributions in abutment regions of intensity modulated radiation therapy and electron fields. *Med Phys*, 29(1):38–44, 2002.

[24] F.C.P. du Plessis, A. Leal, S. Stathakis, W. Xiong, and C-M. Ma. Characterization of megavoltage electron beams delivered through a photon multi-leaf collimator (pMLC). *Phys Med Biol*, 51(8):2113–2129, 2006.

[25] M.A. Ebert and P.W. Hoban. Possibilities for tailoring dose distributions through the manipulation of electron beam characteristics. *Phys Med Biol*, 42(11):2065–2081, 1997.

[26] M. Essers, M. Eggen, D. Binnekamp, C.L. Creutzberg, and B.J. Heijmen. Chest wall irradiation with MLC-shaped photon and electron fields. *Int J Radiat Oncol Biol Phys*, 48(4):1205–1217, 2000.

[27] M. Fippel. Fast Monte Carlo dose calculation for photon beams based on the VMC electron algorithm. *Med Phys*, 26(8):1466–1475, 1999.

[28] M. Fippel, I. Kawrakow, and K. Friedrich. Electron beam dose calculations with the VMC algorithm and the verification data of the NCI working group. *Phys Med Biol*, 42(3):501–520, 1997.

[29] T. Gauer, D. Albers, F. Cremers, R. Harmansa, R. Pellegrini, and R. Schmidt. Design of a computer-controlled multileaf collimator for advanced electron radiotherapy. *Phys Med Biol*, 51(23):5987–6003, 2006.

[30] T. Gauer, J. Sokoll, F. Cremers, R. Harmansa, M. Luzzara, and R. Schmidt. Characterization of an add-on multileaf collimator for electron beam therapy. *Phys Med Biol*, 53(4):1071–1085, 2008.

[31] M.M. Glegg. Electron dose calculations: a comparison of two commercial treatment planning computers. *Med Dosim*, 28(2):99–105, 2003.

[32] S. Goudsmit and J.L. Saunderson. Multiple scattering of electrons. *Phys Rev*, 57:24–29, 1940.

[33] B. Günhan, G. Kemikler, and A. Koca. Determination of surface dose and the effect of bolus to surface dose in electron beams. *Med Dosim*, 28(3):193–198, 2003.

[34] T. Hehr, J. Classen, M. Huth, I. Durst, G. Christ, M. Bamberg, and W. Budach. Postmastectomy radiotherapy of the chest wall. *Strahlenther Onkol*, 180(10):629 – 636, 2004.

[35] P.D. Higgins, B.J. Gerbi, and F.M. Khan. Application of measured pencil beam parameters for electron beam model evaluation. *Med Phys*, 30(4):514–520, 2003.

[36] K.R. Hogström, R.A. Boyd, J.A. Antolak, M.M. Svatos, B.A. Faddegon, and J.G. Rosenman. Dosimetry of a prototype retractable eMLC for fixed-beam electron therapy. *Med Phys*, 31(3):443–462, 2004.

[37] S. Hyödynmaa. *Implementation of the generalised Gaussian pencil beam algorithm for three-dimensional electron beam dose planning*. Doctoral dissertation, Technical Research Centre of Finland Publications 74. Technical Research Centre of Finland, Espoo, Finland, 1991.

[38] S. Hyödynmaa, A. Gustafsson, and A. Brahme. Optimization of conformal electron beam therapy using energy- and fluence-modulated beams. *Med Phys*, 23(5):659–666, 1996.

[39] International Atomic Energy Acency (IAEA). *Absorbed Dose Determination in External Beam Radiotherapy, An International Code of Practice for Dosimetry Based on Standards of Absorbed Dose to Water*. Technical Report Series No. 398. IAEA, Vienna, 2000.

[40] T. Jansson, H. Lindman, K. Nygård, C.V. Dahlgren, A. Montelius, C. Öberg-Kreuger, S. Asplund, and J. Berg. Radiotherapy of breast cancer after breast-conserving surgery an improved technique using mixed electron-photon beams with a multileaf collimator. *Radiother Oncol*, 46(1):83–89, 1998.

[41] S.B. Jiang, A. Kapur, and C.-M. Ma. Electron beam modeling and commissioning for Monte Carlo treatment planning. *Med Phys*, 27(1):180–191, 2000.

[42] M. Karlsson, H. Nystrom, and H. Svensson. Electron beam characteristics of the 50-MeV racetrack microtron. *Med Phys*, 19(2):307–315, 1992.

[43] M. Karlsson and B. Zackrisson. Matching of electron and photon beams with a multi-leaf collimator. *Radiother Oncol*, 29(3):317–326, 1993.

[44] M.G. Karlsson and M. Karlsson. Electron beam collimation with focused and curved leaf end MLCs—experimental verification of Monte Carlo optimized designs. *Med Phys*, 29(4):631–637, 2002.

[45] M.G. Karlsson, M. Karlsson, and C.M. Ma. Treatment head design for multileaf collimated high-energy electrons. *Med Phys*, 26(10):2161–2167, 1999.

[46] M.G. Karlsson, M. Karlsson, and B. Zackrisson. Intensity modulation with electrons: calculations, measurements and clinical applications. *Phys Med Biol*, 43(5):1159–1169, 1998.

[47] C.J. Karzmark. *Medical electron accelerators*. McGraw-Hill, New York, 1993.

[48] I. Kawrakow. Electron transport: lateral and longitudinal correlation algorithm. *Nucl Instrum Methods B*, 114(3-4):307–326, 1996.

[49] I. Kawrakow. Electron transport: multiple and plural elastic scattering. *Nucl Instrum Methods B*, 108:23–34, 1996.

[50] I. Kawrakow. Improved modeling of multiple scattering in the Voxel Monte Carlo model. *Med Phys*, 24(4):505–517, 1997.

[51] I. Kawrakow. Accurate condensed history Monte Carlo simulation of electron transport. I. EGSnrc, the new EGS4 version. *Med Phys*, 27(3):485–498, 2000.

[52] I. Kawrakow. *VMC++. Electron and Photon Monte Carlo Calculations Optimized for Radiation Treatment Planning*. Advanced Monte Carlo for Radiation Physics, Particle Transport Simulation and Applications: Proceedings of the Monte Carlo 2000 Conference. Springer, Berlin, 2001.

[53] I. Kawrakow and A.F. Bielajew. On the condensed history technique for electron transport. *Nucl Instrum Phys Res*, 142(3):253–280, 1998.

[54] I. Kawrakow and M. Fippel. Investigation of variance reduction techniques for Monte Carlo photon dose calculation using XVMC. *Phys Med Biol*, 45(8):2163–2183, 2000.

[55] I. Kawrakow, M. Fippel, and K. Friedrich. 3D electron dose calculation using a Voxel based Monte Carlo algorithm (VMC). *Med Phys*, 23(4):445–457, 1996.

[56] I. Kawrakow, M. Fippel, and K. Friedrich. The effect of Monte Carlo statistical uncertainties on the evaluation of dose distributions in radiation treatment planning. *Phys Med Biol*, 49(8):1549–1556, 2004.

[57] I. Kawrakow and D.W.O. Rogers. *The EGSnrc code system: Monte Carlo simulation of electron and photon transport (NRC C Report PIRS-701).* Ionizing Radiation Standards, National Research Council of Canada, Ottawa, 2003 (Online: http://www.irs.inms.nrc.ca/inms/irs/EGSnrc/EGSnrc.html).

[58] P.J. Keall, J.V. Siebers, R. Jeraj, and R. Mohan. The effect of dose calculation uncertainty on the evaluation of radiotherapy plans. *Med Phys*, 27(3):478–484, 2000.

[59] F.M. Khan, K.P. Doppke, K.R. Hogstrom, G.J. Kutcher, R. Nath, S.C. Prasad, J.A. Purdy, M. Rozenfeld, and B.L. Werner. Clinical electron-beam dosimetry: Report of AAPM Radiation Therapy Committee Task Group No. 25. *Med Phys*, 18(1):73–109, 1991.

[60] E.E. Klein. Modulated electron beams using multi-segmented multileaf collimation. *Radiother Oncol*, 48(3):307–311, 1998.

[61] E.E. Klein, Z. Li, and D.A. Low. Feasibility study of multileaf collimated electrons with a scattering foil based accelerator. *Radiother Oncol*, 41(2):189–196, 1996.

[62] E.E. Klein, D.A. Low, and J.A. Purdy. Changes in electron beam dosimetry with a new scattering foil-applicator system on a CL2100C. *Int J Radiat Oncol Biol Phys*, 32(2):483–490, 1995.

[63] E.E. Klein, M. Mamalui-Hunter, and D.A. Low. Delivery of modulated electron beams with conventional photon multi-leaf collimators. *Phys Med Biol*, 54(2):327–39, 2009.

[64] E.E. Klein, M. Vicic, C.M. Ma, D.A. Low, and R.E. Drzymala. Validation of calculations for electrons modulated with conventional photon multileaf collimators. *Phys Med Biol*, 53(5):1183–208, 2008.

[65] E.V. Korevaar, H. Huizenga, J. Lof, J.C. Stroom, J.W. Leer, and A. Brahme. Investigation of the added value of high-energy electrons in intensity-modulated radiotherapy: four clinical cases. *Int J Radiat Oncol Biol Phys*, 52(1):236–253, 2002.

[66] E.V. Korevaar, R.J. van Vliet, E. Woudstra, B.J. Heijmen, and H. Huizenga. Sharpening the penumbra of high energy electron beams with low weight narrow photon beams. *Radiother Oncol*, 48(2):213–220, 1998.

[67] R.J. Kudchadker, K.R. Hogström, A.S. Garden, M.D. McNeese, R.A. Boyd, and J.A. Antolak. Electron conformal radiotherapy using bolus and intensity modulation. *Int J Radiat Oncol Biol Phys*, 53(4):1023–1037, 2002.

[68] R.G. Kurup, S. Wang, and G.P. Glasgow. Field matching of electron beams using plastic wedge penumbra generators. *Phys Med Biol*, 37(1):145–153, 1992.

[69] M.C. Lee, J. Deng, J. Li, S.B. Jiang, and C-M. Ma. Monte Carlo based treatment planning for modulated electron beam radiation therapy. *Phys Med Biol*, 46(8):2177–2199, 2001.

[70] M.C. Lee, S.B. Jiang, and C.-M. Ma. Monte Carlo and experimental investigations of multileaf collimated electron

beams for modulated electron radiation therapy. *Med Phys*, 27(12):2708–2718, 2000.

[71] J.G. Li, L. Xing, A.L. Boyer, R.J. Hamilton, D.R. Spelbring, and J.V. Turian. Matching photon and electron fields with dynamic intensity modulation. *Med Phys*, 26(11):2379–2384, 1999.

[72] E.P. Lief. Light and electron radiation fields' coincidence at extended distance. *Med Phys*, 29(10):2213–2215, 2002.

[73] R. Loevinger, C.J. Karzmark, and M. Weissbluth. Radiation therapy with high-energy electrons: I. Physical considerations, 10 to 60 MeV. *Radiology*, 77(Dec):906–927, 1961.

[74] D.A. Low, W.B. Harms, S. Mutic, and J.A. Purdy. A technique for the quantitative evaluation of dose distributions. *Med Phys*, 25(5):656–661, 1998.

[75] D.A. Low, G. Starkschall, S.W. Bujnowski, L.L. Wang, and K.R. Hogstrom. Electron bolus design for radiotherapy treatment planning: Bolus design algorithms. *Med Phys*, 19(1):115–124, 1992.

[76] D.A. Low, G. Starkschall, N.E. Sherman, S.W. Bujnowski, J.R. Ewton, and K.R. Hogstrom. Computer-aided design and fabrication of an electron bolus for treatment of the paraspinal muscles. *Int J Radiat Oncol Biol Phys*, 33(5):1127–1138, 1995.

[77] C. Ma, J. Li, L. Jin, A. ElDib, J. Fan, R.A. Price, G. Freedman, P. Anderson, and N. Nicolaou. Advanced mixed beam treatment techniques for breast and head and neck cancers. *Int J Radiat Oncol Biol Phys*, 69(3):S47, 2007.

[78] C-M. Ma, M. Ding, J.S. Li, M.C. Lee, T. Pawlicki, and J. Deng. A comparative dosimetric study on tangential photon beams, intensity-modulated radiation therapy (IMRT) and modulated electron radiotherapy (MERT) for breast cancer treatment. *Phys Med Biol*, 48(7):909–924, 2003.

[79] C-M. Ma, J.S. Li, S.B. Jiang, T. Pawlicki, W. Xiong, L.H. Qin, and J. Yang. Effect of statistical uncertainties on Monte Carlo treatment planning. *Phys Med Biol*, 50(5):891–907, 2005.

[80] C.-M. Ma, E. Mok, A. Kapur, T. Pawlicki, D. Findley, S. Brain, K. Forster, and A.L. Boyer. Clinical implementation of a Monte Carlo treatment planning system. *Med Phys*, 26(10):2133–2143, 1999.

[81] C-M. Ma, T. Pawlicki, M.C. Lee, S.B. Jiang, J.S. Li, J. Deng, B. Yi, E Mok, and A.L. Boyer. Energy- and intensity-modulated electron beams for radiotherapy. *Phys Med Biol*, 45(8):2293–2311, 2000.

[82] C.M. Ma, B.A. Faddegon, D.W.O. Rogers, and T.R. Mackie. Accurate characterization of Monte Carlo calculated electron beams for radiotherapy. *Med Phys*, 24(3):401–416, 1997.

[83] C.M. Ma and S.B. Jiang. Monte Carlo modelling of electron beams from medical accelerators. *Phys Med Biol*, 44(12):R157–R189, 1999.

[84] C.M. Ma, R.A. Price Jr, J.S Li, L. Chen, L. Wang, E. Fourkal, L. Qin, and J. Yang. Monitor unit calculation for Monte Carlo treatment planning. *Phys Med Biol*, 49(9):1671–1687, 2004.

[85] M.E. Masterson, C.S. Chui, R. Febo, J.D. Hung, Z. Fuks, R. Mohan, C.C. Ling, G.J. Kutcher, S. Bjork, and J. Enstrom. Beam characteristics of a new generation 50 MeV racetrack microtron. *Med Phys*, 22(6):781–792, 1995.

[86] A.S. Meigooni, S.A. Parker, J. Zheng, K.J. Kalbaugh, W.F. Regine, and M. Mohiuddin. Dosimetric characteristics with spatial fractionation using electron grid therapy. *Med Dosim*, 27(1):37–42, 2002.

[87] S. Mika and G. Christ. Experimentelle validierung eines Monte-Carlo-basierten bestrahlungsplanungssystems

für elektronenstrahlung. *Strahlenther Onkol*, 183(3):150–156, 2007.

[88] J.M. Moran, M.K. Martel, I.A.D. Bruinvis, and B.A. Fraass. Characteristics of scattered electron beams shaped with a multileaf collimator. *Med Phys*, 24(9):1491–1498, 1997.

[89] R.L. Morin, editor. *Monte Carlo simulation in the radiological sciences*. CRC Press, Inc., Boca Raton, 1988.

[90] X. Mu, L. Olofsson, M. Karlsson, R. Sjögren, and B. Zackrisson. Can photon IMRT be improved by combination with mixed electron and photon techniques? *Acta Oncol*, 43(8):727–735, 2004.

[91] R. Nath, P.J. Biggs, F.J. Bova, C.C. Ling, J.A. Purdy, J. van de Geijn, and M.S. Weinhous. AAPM code of practice for radiotherapy accelerators: Report of AAPM Radiation Therapy Task Group No. 45. *Med Phys*, 21(7):1093–1121, 1994.

[92] L. Olofsson, M.G. Karlsson, and M. Karlsson. Effects on electron beam penumbra using the photon MLC to reduce bremsstrahlung leakage for an add-on electron MLC. *Phys Med Biol*, 50(6):1191–1203, 2005.

[93] L. Olofsson, M.G. Karlsson, and M. Karlsson. Photon and electron collimator effects on electron output and abutting segments in energy modulated electron therapy. *Med Phys*, 32(10):3178–3184, 2005.

[94] L. Olofsson, X. Mu, S. Nill, U. Oelfke, B. Zackrisson, and M. Karlsson. Intensity modulated radiation therapy with electrons using algorithm based energy/range selection methods. *Radiother Oncol*, 73(2):223–231, 2004.

[95] International Commission on Radiation Units and Measurements (ICRU). *ICRU Report 71: Prescribing, Recording, and Reporting Electron Beam Therapy*. Journal of the ICRU, 4(1):2–100, 2004.

[96] International Commission on Radiation Units and Measurements (ICRU). *Determination of absorbed dose in a patient irradiated by beams of X or gamma rays in radiotherapy procedures. ICRU Report 24.* ICRU, Bethesda, MD, 1976.

[97] E. Papiez, P.B. Dunscombe, and K. Malaker. Matching photon and electron fields in the treatment of head and neck tumors. *Med Phys*, 19(2):335–341, 1992.

[98] G.H. Perkins, M.D. McNeese, J.A. Antolak, T.A. Buchholz, E.A. Strom, and K.R. Hogstrom. A custom three-dimensional electron bolus technique for optimization of postmastectomy irradiation. *Int J Radiat Oncol Biol Phys*, 51(4):1142–1151, 2001.

[99] I.A. Popescu, C.P. Shaw, S.F. Zavgorodni, and W.A. Beckham. Absolute dose calculations for Monte Carlo simulations of radiotherapy beams. *Phys Med Biol*, 50(14):3375–3392, 2005.

[100] B.P. Ravindran, I.R.R. Singh, S. Brindha, and S. Sathyan. Manual multi-leaf collimator for electron beam shaping - a feasibility study. *Phys Med Biol*, 47(24):4389–4396, 2002.

[101] D.W.O. Rogers. Monte Carlo techniques in radiotherapy. *Physics in Canada*, 58(2):63–70, 2002.

[102] D.W.O. Rogers, B.A. Faddegon, G.X. Ding, C.-M. Ma, J. We, and T.R. Mackie. BEAM: A Monte Carlo code to simulate radiotherapy treatment units. *Med Phys*, 22(5):503–524, 1995.

[103] D.W.O. Rogers, B. Walters, and I. Kawrakow. *BEAMnrc Users Manual (NRCC Report PIRS-0509 ArevK).* Ionizing Radiation Standards, National Research Council of Canada, Ottawa, 2006 (Online: http://www.irs.inms.nrc.ca/BEAM/user_manuals/pirs0509/index.html).

[104] S.N. Rustgi and K.R. Working. Dosimetry of small field electron beams. *Med Dosim*, 17(2):107–110, 1992.

[105] F. Salvat, J.M. Fernández-Varea, and J. Sempau. *PENELOPE-2006: A Code System for Monte Carlo Simulation of Electron and Photon Transport*. Workshop Proceedings Barcelona, Spain, 4-7 July 2006. OECD, 2006, (Online: http://www.oecd-nea.org/science/pubs/2006/nea6222-penelope.pdf).

[106] A. Samuelsson, S. Hyödynmaa, and K.A. Johansson. Dose accuracy check of the 3D electron beam algorithm in a treatment planning system. *Phys Med Biol*, 43(6):1529–1544, 1998.

[107] C. Scherf, J. Scherer, and L. Bogner. Verifikation und anwendungen des voxelbasierten Monte-Carlo-(VMC++) elektronen-dosismoduls von Oncentra$^{\mathrm{TM}}$ MasterPlan. *Strahlenther Onkol*, 183(2):81–88, 2007.

[108] S.C. Sharma, M.W. Johnson, and M.S. Gossman. Practical considerations for electron beam small field size dosimetry. *Med Dosim*, 30(2):104–106, 2000.

[109] B.B. Sorcini, S. Hyödynmaa, and A. Brahme. The role of phantom and treatment head generated bremsstrahlung in high-energy electron beam dosimetry. *Phys Med Biol*, 41(12):2657–2677, 1996.

[110] M. Tenhunen, H. Nyman, S. Strengell, and L. Vaalavirta. Linac–based isocentric electron–photon treatment of radically operated breast carcinoma with enhanced dose uniformity in the field gap area. *Radiother Oncol*, 93(1):80–6, 2009.

[111] E. Traneus, A. Ahnesjö, M. Fippel, I. Kawrakow, F. Nusslin, G. Zeng, and M. Åsell. Application and verification of a coupled multi-source electron beam model for Monte Carlo based treatment planning. The 6th Biennial ESTRO Meeting, Sevilla 2001. *Radiother Oncol*, 61(Suppl. 1):S102, 2001.

[112] E. Traneus, T. Vatanen, and T. Lahtinen. Beam model for multi-leaf collimated high-energy electron beams. The ESTRO25 Meeting, Leipzig 2006. *Radiother Oncol*, 81(Suppl. 1):S28, 2006.

[113] K. Ulin and M. Palisca. The use of scattering foil compensators in electron beam therapy. *Int J Radiat Oncol Biol Phys*, 35(4):785–792, 1996.

[114] A. Väänänen. *Theoretical and Experimental Study on Transition Zone Dosimetry with Special Reference to Skin Dose Measurement with Low Megavoltage Beams*. Doctoral dissertation, Kuopio University Publications C. Natural and Environmental Sciences 142. University of Kuopio, Kuopio, Finland, 2002.

[115] L.J. van Battum, W. van der Zee, and H. Huizenga. Scattered radiation from applicators in clinical electron beams. *Phys Med Biol*, 48(15):2493–2507, 2003.

[116] H.P. van der Laan, W.V. Dolsma, A.A. van't Veld, H.P. Bijl, and J.A. Langendijk. Comparison of normal tissue dose with three-dimensional conformal techniques for breast cancer irradiation including the internal mammary nodes. *Int J Radiat Oncol Biol Phys*, 63(5):1522–1530, 2005.

[117] T. Vatanen, E. Traneus, and T. Lahtinen. A new add-on electron multi-leaf collimator (eMLC): dosimetry and dose calculation using a new beam model with Voxel Monte Carlo. The ESTRO25 Meeting, Leipzig 2006. *Radiother Oncol*, 81((Suppl. 1)):S102, 2006.

[118] F. Verhaegen, C. Mubata, J. Pettingell, A.M. Bidmead, I. Rosenberg, D. Mockridge, and A.E. Nahum. Monte Carlo calculation of output factors for circular, rectangular, and square fields of electron accelerators (6–20 MeV). *Med Phys*, 28(6):938–949, 2001.

[119] F. Verhaegen and J. Seuntjens. Monte Carlo modelling of external radiotherapy photon beams. *Phys Med Biol*, 48(21):R107–R164, 2003.

[120] B. Walters, I. Kawrakow, and D.W.O. Rogers. *DOSXYZnrc Users Manual (NRCC Report PIRS-794revB)*. Ionizing Radiation Standards, National

Research Council of Canada, Ottawa, 2006 (Online: http://www.irs.inms.nrc.ca/BEAM/user_manuals/pirs794/index.html).

[121] M.M. Xu, A. Sethi, and G.P. Glasgow. Dosimetry of small circular fields for 6-MeV electron beams. *Med Dosim*, 34(1):51–56, 2009.

[122] B. Zackrisson and M. Karlsson. Matching of electron beams for conformal therapy of target volumes at moderate depths. *Radiother Oncol*, 39(3):261–270, 1996.

[123] G.G. Zhang, D.W.O. Rogers, J.E. Cygler, and T.R. Mackie. Monte Carlo investigation of electron beam output factors versus size of square cutout. *Med Phys*, 26(5):743–750, 1999.

[124] M. Åsell, S. Hyödynmaa, A. Gustafsson, and A. Brahme. Optimization of 3D conformal electron beam therapy in inhomogeneous media by concomitant fluence and energy modulation. *Phys Med Biol*, 42(11):2083–2100, 1997.

# ORIGINAL PUBLICATIONS

**Tero Vatanen**

# *Multi-leaf Collimation of Electron Beams with Monte Carlo Modelling and Dose Calculation*

*Special Reference to Dosimetry and Build-up Dose*

Megavoltage electron beams have been applied to treat superficial target volumes throughout the past few decades of modern radiotherapy. The new and promising leaf-based collimators aim at more practical beam delivery. Together with the new beam models and fast Monte Carlo simulation methods, the accuracy of dose calculations is improved without markedly increasing the required computational resources and time in clinical situations.

UNIVERSITY OF
EASTERN FINLAND

Publications of the University of Eastern Finland
*Dissertations in Forestry and Natural Sciences*

ISBN 978-952-61-0433-1